Draft version November 15, 2025
Typeset using LaTeX **twocolumn** style in AASTeX63

# Steady Warps: Linear, Nonlinear, and Breaking

Jiaru Li [1] and Yoram Lithwick [1, 2]

[1] *Center for Interdisciplinary Exploration and Research in Astrophysics (CIERA), Northwestern University, 1800 Sherman Ave, Evanston, IL 60201, USA*

[2] *Department of Physics and Astronomy, Northwestern University, 2145 Sheridan Rd, Evanston, IL 60208, USA*

## ABSTRACT

An increasing number of protoplanetary disks shows observational signatures of warps and misalignments, raising questions of how disks sustain coherent warps and how they may break into misaligned pieces. We study the steady-state structures and breaking conditions of warped disks. To focus on the hydrodynamics, while remaining agnostic about what forces the warp, we adopt a simple but physically motivated setup: rather than including an explicit perturber or external torque, we fix the disk inclination angles $\beta_{\rm in}$ and $\beta_{\rm out}$ at the inner and outer boundaries. The disk is hence constrained to accommodate a warp between the boundaries. By varying the boundary misalignment $|\beta_{\rm out} - \beta_{\rm in}|$, we can explore the linear regime, the nonlinear regime, and the onset of breaking, while having good control over the warp amplitude. Combining this model with analytical theories and three-dimensional hydrodynamic simulations, we carry out a clean and systematic investigation of the hydrodynamic behaviors of warped disks. We find that, with small warps, disks settle into warp steady states that are well described by the linear theory. Moderately warped disks enter the nonlinear regime, showing several distinct features such as torque saturation, vertical "bouncing" motion of gas, and enhanced mass accretion rates. Measurements of these effects in our simulations show good quantitative agreement with nonlinear theories. Strongly warped disks are unstable: these disks are susceptible to a runaway growth of warp amplitude that ultimately leads to disk breaking. This instability may be caused by the nonlinear saturation of the disk internal torque, which occurs roughly when the warp amplitude exceeds a critical value $|\psi|_{\rm crit} \simeq 2\sqrt{\alpha}$ for Keplerian disks.

## 1. INTRODUCTION

Accretion disks are not always flat; gas circulating the same central object at different radii may have different orbital inclinations, producing warped structures.

Recent observations have found an increasing amount of evidence that such warps commonly exist in protoplanetary disks. In near-infrared scattered light images, many disks exhibit non-axisymmetric dark regions (e.g., Marino et al. 2015; Stolker et al. 2017; Benisty et al. 2018; Casassus et al. 2018; Muro-Arena et al. 2020; Keppler et al. 2020; Kraus et al. 2020), which is often interpreted as shadows cast by warps (see Benisty et al. 2023). Complementary evidence comes from molecular line observations, through which several disks are found to have large-scale $m = 1$ velocity structures consistent with warped or non-planar gas flows (e.g., Panić et al. 2010; Pineda et al. 2014; Casassus et al. 2015; Winter et al. 2025). In addition, increasingly many systems have been revealed to host both warps and multiple misaligned disk components, pointing to a rich dynamical history involving both disk bending and breaking (e.g., Kraus et al. 2020; Muro-Arena et al. 2020; Bohn et al. 2022). Together, these observations raise two fundamental questions: how do disks bend and sustain coherent warps, and under what circumstances do they break into misaligned components?

Theories of warped disks have been developed over the past several decades (see, e.g., Nixon & King 2016, for an overview). In these studies, a warp is formally defined as the radial derivative of the disk inclination. Misaligned disk annuli can exert internal torques on each other (due to pressure, etc), which in turn drives the changes of the inclination profiles of the whole disk.

For nearly-Keplerian disks, how warp evolves depends on the viscous parameter $\alpha$ (Shakura & Sunyaev 1973) relative to the disk aspect ratio $h \equiv H/R$. Linear theories show that, for $\alpha \lesssim h$, warps can propagate as bending waves at approximately half of the sound speed, while being viscously damped at a rate $\sim \alpha\Omega$, where $\Omega$ is the angular velocity of the gas (Papaloizou & Lin 1995; Lubow & Ogilvie 2000). When $\alpha \gtrsim h$, viscous damping becomes strong enough to suppress wave propagation, so the warp instead evolves in a diffusive manner (Papaloizou & Pringle 1983). As a result, in the absence of external torques, free warps tend to flatten on the in-

DRAFT

termediate timescale between the orbital period $\sim \Omega^{-1}$ and the global viscous timescale $\sim (\alpha h^2 \Omega)^{-1}$. Warps in forced disks, on the other hand, may settle into steady states on the intermediate timescale if the relevant forcing acts more slowly (e.g., Lubow & Ogilvie 2000; Foucart & Lai 2014). Note that, if $\alpha$ is negligible, the evolution becomes sensitive to the difference between orbital and epicylic frequencies (i.e., the non-Keplerianity, see e.g., Ogilvie 1999, or Section 2). Hydrodynamic simulations have found good agreement with these linear theories (e.g., Lodato & Pringle 2007; Lodato & Price 2010; Kimmig & Dullemond 2024; Fairbairn 2025) .

The nonlinear regime, where warp amplitudes are large, is more complex and less well understood. Analytical theories predict several important nonlinear effects, such as modifications of the internal torques (Ogilvie 1999; Ogilvie & Latter 2013a; Dullemond et al. 2022), changes to the mass accretion flow (e.g., Pringle 1992; Ogilvie 1999), and the so-called "bouncing effect", in which gas elements would perform rapid vertical compression and expansion as they orbit around the star (Ogilvie & Latter 2013a; Fairbairn & Ogilvie 2021a,b; Held & Ogilvie 2024). These features have been identified in several numerical simulations (e.g., Lodato & Price 2010; Sorathia et al. 2013; Deng & Ogilvie 2022; Kaaz et al. 2023, 2025; Kimmig & Dullemond 2024). In low-$\alpha$ disks, wave coupling can also lead to parametric instability (Gammie et al. 2000; Ogilvie & Latter 2013b), which was not seen in the early numerical studies but emerged in recent high-resolution simulations (e.g., Paardekooper & Ogilvie 2019; Deng et al. 2021; Deng & Ogilvie 2022; Fairbairn & Stone 2025). Due to the complex nature of nonlinear hydrodynamics, recent studies tend to either pursue more powerful simulations (e.g., Deng & Ogilvie 2022; Kaaz et al. 2025) or develop alternative frameworks, such as affine models (Ogilvie 2018) and ring models (Fairbairn & Ogilvie 2021a).

Extreme nonlinear evolution can lead to disk breaking, where the disk splits into multiple disconnected planes (e.g., Larwood et al. 1996; Nixon et al. 2012, 2013; Zhu 2019; Liska et al. 2021). Several theories have been proposed to explain the mechanisms of breaking, including resonance with tidal forcing (Lubow & Ogilvie 2000; Martin et al. 2020), rapid nodal precession (Zhu 2019; Martin et al. 2020; Rabago et al. 2024), and linear instabilities related to the anti-diffusion of the disk density (Doğan et al. 2018; Raj et al. 2021). Yet a general condition and physical mechanisms that trigger disk breaking remain unclear.

In this paper, we focus on the long-lived warp steady state (WSS). Such states are more likely to be observable than their transient predecessors: given the lifetimes of protoplanetary disks, any warps present are likely to have relaxed into quasi-steady configurations. Our primary goals are to determine the WSS structures of disks, both in the linear and the nonlinear regimes, and to diagnose how a sufficiently large warp drives disk breaking.

We perform both theoretical analysis and numerical simulations. To focus on the hydrodynamics, while remaining agnostic about what forces the warp, we adopt a simple but physically motivated setup: rather than include an explicit perturber or external torque, we fix the disk inclination angles $\beta_{\rm in}$ and $\beta_{\rm out}$ at the inner and outer boundaries. The disk is hence constrained to accommodate a warp between the boundaries, and we can study the resulting steady-state structure. In the simulations, we also lower the surface density in the middle of the disk (but keep it non-empty), allowing us to localize the warp and reduce the possible influence of artificial boundary conditions. Our setup provides a clean laboratory for testing the hydrodynamic response of disks to generic perturbations. By varying the boundary misalignment $|\beta_{\rm out} - \beta_{\rm in}|$, we can explore the linear regime, nonlinear regime, and the onset of breaking, while having good control over the warp amplitude. As we will show, our simulations show excellent agreement with the theories.

The rest of this paper is organized as follows. In Section 2, we review the linear theory of warped disks. We use hydrodynamic simulations to study the steady-state warp in the linear and nonlinear regimes in Sections 3 and 4, respectively. In Section 5, we investigate the conditions of disk breaking. Finally, we conclude in Section 6.

## 2. LINEAR THEORY

### 2.1. *Equations of Motion*

We focus on a disk with a steady warp (Figure 1). We imagine that the disk is forced to have unequal inclinations at its inner and outer boundaries, and study the resulting inclination profile in between. As discussed above, the timescale for the disk's inclination to reach its steady profile is much shorter than the disk's viscous time, and so in this section we regard the surface density profile as a given time-independent function of radius.

The equations for the inclination have been derived many times (Pringle 1992; Ogilvie 1999; Fairbairn 2025, etc). We derive them again in Appendix A, because our assumption of a steady warp facilitates a conceptually simpler derivation, and allows us to proceed from first principles. Our derivation also makes clear that the resulting steady equations are equally valid whether

DRAFT

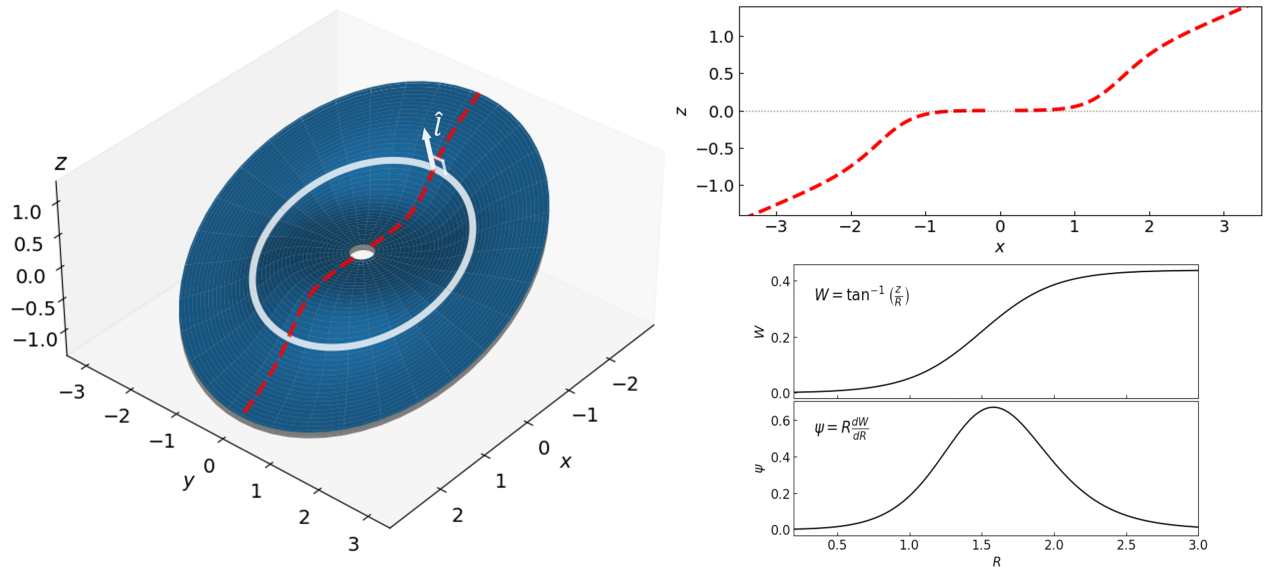


**Figure 1.** Midplane of a warped disk. This disk has no twist ($W$ is purely real). **Left:** 3D diagram of the disk. The red dashed curve marks the maximum $|z|$ at each $R$, which lies along $y = 0$ for this untwisted disk. The white circle marks the location of the disk midplane at $r = 1.75$, while the arrow represents the direction of the tilting vector $\hat{\boldsymbol{l}}$ at this radius. **Right Top:** Same as red-dashed curve in left panel. **Right Bottom:** Inclination and warp.

$\alpha < h$ or $\alpha > h$, i.e., in the "wave-like" or "diffusive" regimes. Here we summarize the derivation, highlighting the physical interpretation.

In this section, we adopt cylindrical coordinates $(R, \phi, z)$, a globally isothermal equation of state, and an $\alpha$ viscosity. We first solve for an unperturbed disk that is axisymmetric and aligned with the $z$ axis. We then perturb the equations of motion to linear order, and assume that perturbed variables take on an $m = 1$ dependence in $\phi$, and that their dependence on $z$ is the leading term in a Hermite expansion. Higher-order Hermite terms, which have smaller vertical wavelengths, are suppressed by powers of the disk aspect ratio

$$h \equiv H/R \tag{1}$$

where $H$ is the scale height. The perturbed radial and vertical velocities are then expressed as

$$\frac{v_R'}{\Omega R} = U_R \frac{z}{H} e^{-i\phi}, \tag{2}$$

$$\frac{v_z'}{\Omega R} = U_z e^{-i\phi}, \tag{3}$$

where the coefficients $U_R$ and $U_z$ are functions only of $R$, $\Omega(R)$ is the unperturbed angular frequency (Equation A12), which for a globally isothermal disk is independent of $z$. Analogous expressions apply for $v_\phi'$ and the perturbed density (Equations A22 and A24). The resulting equations are reduced to two coupled equations for $U_R$ and $U_z$ (Equations A30 and A31). For reasons to be discussed shortly, we change dependent variables to

$$W \equiv -iU_z \tag{4}$$

$$U_r \equiv U_R + hU_z. \tag{5}$$

The resulting linear equations of motion are then

$$\frac{d}{dR}\left(\Sigma H R^3 \Omega^2 U_r\right) = 0, \tag{6}$$

$$(2\alpha + i\epsilon)\, U_r = H\frac{dW}{dR}, \tag{7}$$

where $\Sigma$ is the imposed surface density, and $\epsilon$ quantifies the deviation of the epicyclic frequency from its Keplerian value. The expression for $\epsilon$ is given by Equation A13; it is typically small ($O(h^2)$), but can become big if $d\Sigma/dR$ is big. Rayleigh stability necessitates $\epsilon > -1$.

The variables $W$ and $U_r$ have clear physical interpretations. The former is the complex inclination. In other words, the disk's unit normal $\hat{\boldsymbol{l}}$ is, in Cartesian $[x, y, z]$ components

$$\hat{\boldsymbol{l}} \approx [\mathrm{Re}(W), \mathrm{Im}(W), 1] \tag{8}$$

to linear order in $W$.[1] Figure 1 (left panel) depicts the midplane of a warped disk with purely real $W$, meaning

[1] In what follows, we shall define $\hat{\boldsymbol{l}}$ more precisely, as the unit vector that is in the direction of the angular momentum of a spherical shell. See Equation (B49) in the Appendix B.2 for the full definition. We also show in that appendix that the resulting $\hat{\boldsymbol{l}}$ is given by Equation (8), to linear order in $W$, after dropping $\mathcal{O}(hW)$ and $\mathcal{O}(h^2\psi/(2\alpha + i\epsilon))$ corrections.

that it is not twisted. In this case, the maximum height at each radius lies at $y = 0$, as depicted by the dashed red line, which is repeated in the top right panel. The lower-right panels show the $W$ profile, which in this case of real $W$ is the usual (real-valued) inclination, and its warp $\psi$. For general complex $W$, the complex-valued warp is defined as

$$\psi \equiv \frac{dW}{d\ln R}. \tag{9}$$

In the figure, the warp is concentrated around $R \sim 1.5$. At much smaller or bigger $R$, the disk is unwarped, meaning that the disk tends to a flat plate, in which the inclination $W$ is constant, and the maximum $z$ is proportional to $x$.

The variable $U_r$ quantifies sloshing motions that are in the "disk-horizontal" direction, i.e., perpendicular to $\hat{\boldsymbol{l}}$. As shown in Appendix A.3, the radial speed in the (spherical) $\hat{\boldsymbol{r}}$ direction is

$$\frac{v_r'}{\Omega R} = U_r \frac{z}{H} e^{-i\phi'} \ , \tag{10}$$

(after dropping $O(h^2)$ corrections) i.e., it has amplitude $U_r$. The dependence on $z$ in Equation (10) indicates sloshing, in that the nearly-horizontal motion has an antisymmetric profile in $z$.[2] The sloshing is closely related to the torque (Lubow & Ogilvie 2000), as will be described in more detail in Section 3.4.

We turn now to the interpretation of the two linear equations. Equation (6) states that the torque is independent of $R$. Equation (7) states that the warp $\psi = dW/d\ln R$ drives sloshing. The dynamics may be appreciated by considering two neighboring circular rings in the midplane of a warped disk. Since their normals $\hat{\boldsymbol{l}}$ differ, from the perspective of one ring its neighbor moves up and down. That causes a disk-horizontal pressure gradient, which in turn forces the sloshing (see, e.g., discussion in Ogilvie & Latter 2013a, and their Figure 5). Equation (7) shows that for a given warp, the sloshing is $\propto 1/(2\alpha + i\epsilon)$, which is almost always very large in magnitude. The reason for this extreme reaction is that the vertical motions that accompany the warp are nearly resonant with free sloshing (epicyclic-type) motions in a nearly Keplerian disk (e.g., Papaloizou & Pringle 1983; Ogilvie 1999).

[2] The reason $v_r'$ rather than $v_R'$ is relevant for sloshing may be appreciated by considering an unwarped disk (a flat plate) that is inclined relative to the $z = 0$ plane. In that case, $v_r' = 0$ as it is for an uninclined plate. But $v_R' \neq 0$ because inclining the disk introduces velocities in the $R$-direction that have the same $z$ and $\phi$-dependence as Equation (2).

As discussed below, the linear equations break down when the warp is sufficiently big, $|\psi| \gtrsim \sqrt{\alpha}$ (ignoring $\epsilon$). When that happens, the sloshing equation (Equation (7)) changes. We shall show that much—but not all—of the change is captured by the local nonlinear model of Ogilvie & Latter (2013a).

### 2.2. *Solution of the Linear Equations*

We rewrite the linear equations in terms of

$$G \equiv -\frac{1}{2}\Sigma H R^3 \Omega^2 U_r, \tag{11}$$

which implies

$$\frac{dG}{dR} = 0, \tag{12}$$

$$(4\alpha + 2i\epsilon)\, G = -\Sigma H^2 R^3 \Omega^2 \frac{dW}{dR}. \tag{13}$$

We show in Section 3.4 that $G$ represents the torque. The first equation has solution $G = \text{const}$. The second can then be integrated for the $W(R)$ profile. The boundary conditions are subtler. If the disk is not subject to external forcing, then $G = 0$ at the boundaries, and the steady solution is trivial, $W = \text{const}$, i.e., the disk is a flat plate, with constant inclination. On the other hand, an external perturber such as a planet or the outer disk can apply a torque, forcing $G$. The details depend on the perturber. But since we are interested in the disk's inclination profile rather than its interaction with a perturber, we adopt an equivalent, but conceptually slightly different, approach: we fix the inner and outer inclinations, and solve for $W(R)$ in between. Equation (13) gives

$$R\frac{dW}{dR} = \text{const}\frac{2\alpha + i\epsilon}{\Sigma R^2} \tag{14}$$

after adopting our globally isothermal assumption ($c_s = H\Omega = \text{const}$). The right-hand side is a known function of $R$. Without loss of generality, we choose $W = 0$ at the inner boundary, and $W = 1$ at the outer. The latter is general because the problem is linear, and so $W(R)$ scales in proportion to its value at the outer boundary. Equation (13) is then integrated, with the constant in the equation adjusted to match the outer inclination.

Equation (14) shows that the warp is largest where $\Sigma R^2$ is smallest (ignoring $\epsilon$ for now). Intuitively, a smaller $\Sigma$ means that the disk is weaker, and the disk bends primarily where it is weakest. Figure 2 shows some solutions of the linear equations with three different assumed $\Sigma$ profiles, which are shown in the top-left panel. We set the domain to be

$$0.5 < R < 3 \tag{15}$$

DRAFT

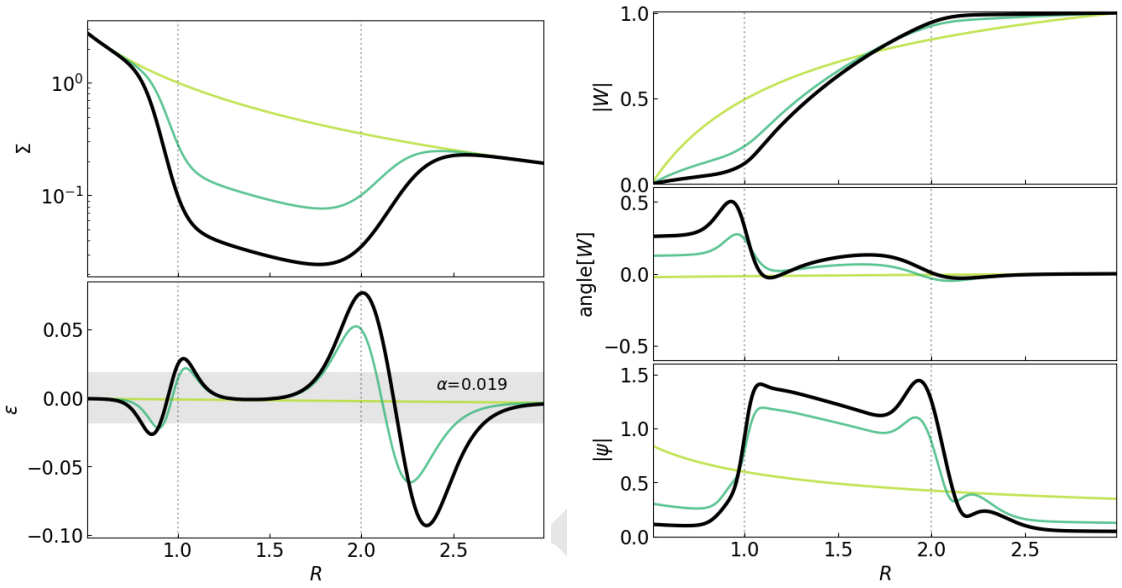


**Figure 2.** Examples of steady-state warp structures for disks with different background profiles. **Upper left:** Background surface density profiles of $\Sigma$. All disks are based on a power-law density $\Sigma \propto R^{-3/2}$, but applied with different density gaps (with gap edges marked with vertical dotted lines). **Lower left:** Background $\epsilon$ profiles calculated based on $\Sigma$; all disks adopts $\alpha = 0.19$, with the gray-shaded region shows where $|\epsilon| < \alpha$. **Top Right:** Steady-state $|W|$ profiles calculated from the linear steady-state Equations (6) and (7); we normalized the results to $|W| = 1$ at the $R = 3R_0$. **Middle Right:** Phase angle of the steady-state complex $W$. **Bottom Right:** Warp amplitude $|\psi|$ based on the $|W|$ profiles. We take the **thick black** case as our fiducial model.

and

$$\alpha = 0.019, \tag{16}$$

$$h = 0.02 \times R^{1/2}, \tag{17}$$

where the latter is needed to obtain $\epsilon$. The green $\Sigma$ profile is a power law, $\Sigma \propto R^{-3/2}$. The resulting $W$ and $\psi$ are shown in the right panels. For this case, the warp $|\psi|$ is dominated at the inner boundary. In general, a power-law $\Sigma$ profile produces a warp that is largest at the boundary.

For the other two $\Sigma$ profiles, we impose gaps of depth 0.2 and 0.05. As a result, the warp is concentrated in the gap, as may be seen in the right panels. For our later comparisons, it will prove convenient to keep the warp away from the domain boundaries, so that it is not affected by uncertain boundary conditions. We will do that by imposing a gap. But imposing a gap introduces a small complication: $\epsilon$ can get large at gap edges, as shown in the lower-left panel. Nonetheless, as long as $|\epsilon| \ll |\alpha|$, as is true within most of the gap for the profiles shown, the effect of $\epsilon$ may be ignored there.

## 3. SIMULATIONS IN THE LINEAR REGIME

### 3.1. *Setup*

We perform 3D hydrodynamics simulations of warped disks using Athena++ (Stone et al. 2020) to study the behavior of disks at different warp amplitudes. The simulations solve the Navier-Stokes equations for a globally isothermal viscous disk in spherical polar coordinates $(r, \theta, \phi)$. The parameters for our simulations are listed in Table 1. Their setup is based on the setup studied in Section 2. The initial surface density profile is the same as the black curve in Figure 2, with a gap in the central region. The disk is then evolved while holding the inner inclination at zero, and the outer inclination

**Table 1.** Simulation parameters. The upper table lists parameter values that are common to all runs. The lower table summarizes run-specific parameters: the outer inclination $\beta_{\rm out}$, the half-width of the domain in $\theta$, and the number of grid points.

| $c_s$ | $\alpha$ | $r$-domain |
|---|---|---|
| 0.02 | 0.019 | $(0.5, 3.0)$ |

| Name | $\beta_{\rm out}$ | $\Delta\theta$ | $(N_r, N_\theta, N_\phi)$ |
|---|---|---|---|
| C03init | 0.033 | 0.24 | $(256, 256, 260)$ |
| C03 | 0.033 | 0.24 | $(256, 256, 260)$ |
| C10 | 0.10 | 0.74 | $(256, 728, 260)$ |
| C15 | 0.15 | 0.74 | $(256, 728, 260)$ |
| C20 | 0.20 | 0.74 | $(256, 728, 260)$ |
| C30 | 0.30 | 0.74 | $(256, 728, 260)$ |
| C40 | 0.40 | 0.74 | $(256, 728, 260)$ |

at a fixed value ($\beta_{\rm out}$). Appendix C.1 details how that is done via boundary conditions. The radial domain is $0.5 < r < 3$, and the domain's angular half-width, $\Delta\theta$, is as listed in the table, as are $c_s$ and $\alpha$. The time unit is chosen so that the Keplerian angular frequency at $r = 1$ is unity. Boundary conditions fix the value of $\Sigma$ at the outer boundary throughout the course of the simulation, and model an inward mass flux through the inner boundary (Appendix C.1)

In this section, we study the time evolution of a small warp, with simulation C03init. This simulation is distinguished from the others in that the initial inclination profile is set arbitrarily, rather than to the solution of the linearized equation.

### 3.2. *Radial Structures: $\Sigma$, $\beta$, and $\psi$*

#### 3.2.1. *Diagnostics*

Our main diagnostics will be the angle angle-averaged surface density,

$$\Sigma = \frac{r}{2\pi}\int \rho\ \sin\theta d\theta d\phi\ , \tag{18}$$

and the angular momentum per unit $r$

$$\boldsymbol{L} = r^2\int \rho \boldsymbol{r}\times\boldsymbol{v}\ \sin\theta d\theta d\phi\ , \tag{19}$$

with both being functions only of $r$ and $t$. From $\boldsymbol{L}$, we define the unit vector

$$\hat{\boldsymbol{l}} = \boldsymbol{L}/|\boldsymbol{L}|\ , \tag{20}$$

and thence the inclination ($\beta$) and longitude of ascending node ($\gamma$) via

$$\hat{\boldsymbol{l}} = [\sin\beta\cos\gamma, \sin\beta\sin\gamma, \cos\beta]\ . \tag{21}$$

We also define the vectorial warp as

$$\boldsymbol{\psi} = \frac{d\hat{\boldsymbol{l}}}{d\ln r} \tag{22}$$

(Ogilvie 1999; Dullemond et al. 2022). Those two vectors are orthogonal, $\hat{\boldsymbol{l}}\cdot\boldsymbol{\psi} = 0$.

As we show in Appendix B, the vectors $\hat{\boldsymbol{l}}$ and $\boldsymbol{\psi}$ are closely related to the complex variables $W$ and $\psi$ used in Section 2. In the limit of small inclinations ($\beta \ll 1$), they are related by

$$W \approx \hat{\boldsymbol{l}}_x + i\hat{\boldsymbol{l}}_y \approx \beta e^{i\gamma} \tag{23}$$

$$\psi \approx \boldsymbol{\psi}_x + i\boldsymbol{\psi}_y \tag{24}$$

where $x$ and $y$ subscripts are the Cartesian components of those vectors. The vectors are more convenient when analyzing the results of simulations, because the complex variables require a reference plane for their definition.[3]

#### 3.2.2. *Results*

For the simulation studied in this section (C03init), the initial inclination profile rises linearly across the domain, from $\beta$ =0 to 0.033, and with no twist ($\gamma = 0$). Snapshots of $\Sigma$ and inclination-related variables at two subsequent times are shown in Figure 3.

The evolution of $\Sigma$ (panel a) is virtually unaffected by the warp in this run, as we have confirmed by comparing with a zero-inclination disk. The viscous time across a distance $r$ is $t_{\rm vis} \approx \alpha^{-1}h^{-2}r^{3/2} \approx 10^5 r^{1/2}$. The evolution timescale of $\Sigma$ seen in Figure 3(a) is faster than that by a factor of around 100, due to the narrowness of the gap edges.

The time for the inclination to reach its steady profile is much shorter than the evolution time of $\Sigma$. There are two relevant warp timescales, one associated with the time for a warp to travel $t_{{\rm warp},c_s} \approx (2r/c_s) = 100r$, and the other for the warp to damp $t_{{\rm warp},\alpha} \approx \alpha^{-1}r^{3/2} = 52r^{3/2}$. Figure 4 shows the time evolution of $\beta$ at the middle of the gap. The initial evolution exhibits a damped oscillation, on a timescale of $\sim 100$, in agreement with the two warp timescales. After that, the inclination evolves much more slowly, on the viscous timescale of $\Sigma$. Therefore beyond a time of $\sim 100$, the steady warp theory (Section 2) should be applicable.

Figure 3(b) shows snapshots of the inclination profile as solid curves, and the theoretical prediction as dotted curves, which is obtained by integrating Equation (14) with the real-time $\Sigma$ and $\epsilon$ and taking $\beta = |W|$. The theory is seen to agree well with the simulations.

Panel (c) is the same as (b), except showing the $\gamma$ profile. The agreement between measured and predicted $\gamma$ is adequate, although worse than for $\beta$. In linear theory, $\gamma$ differs from zero due to the effect of non-Keplerianity ($\epsilon$), as may be seen from the integral of Equation 14, and recalling that $\angle W \approx \gamma$. Thus, the mismatch in panel (c) is likely due to an insufficiently accurate evaluation of $\epsilon$ as the density evolves in time. But since $\gamma$ has a subdominant effect on the warp $|\boldsymbol{\psi}|$, the agreement in panel (c) is not too concerning.

Panel (d) shows the warp profile (Equation 22), demonstrating good agreement with linear theory.

[3] Throughout this paper, $\psi$ denotes the complex-valued quantity, and $|\boldsymbol{\psi}|$ the magnitude of the vector. The same convention applies to complex numbers $G$ and $U_r$, and their corresponding vectors $\boldsymbol{G}$ and $\boldsymbol{U_r}$, where the latter two quantities will be defined below.

DRAFT

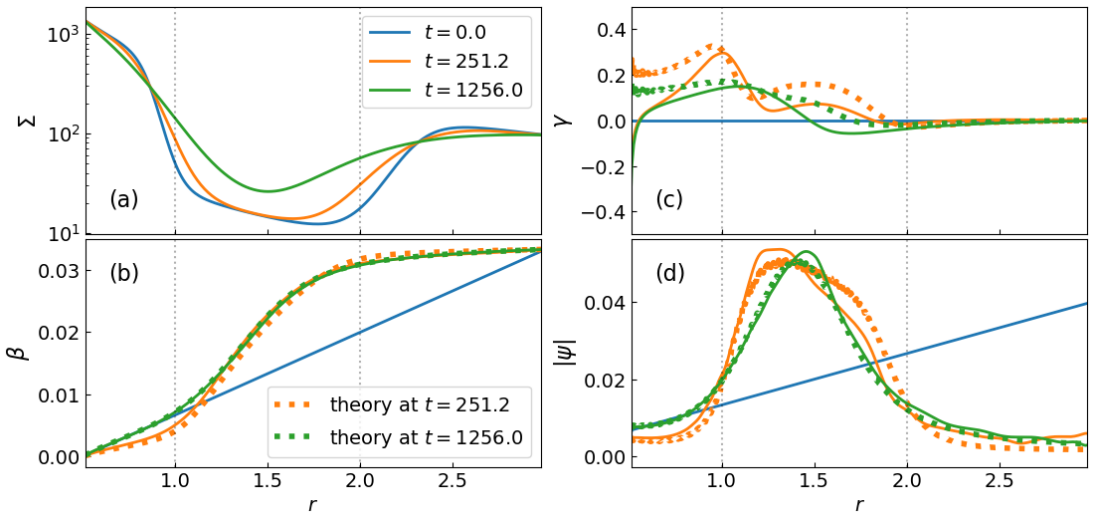


**Figure 3.** Structure evolution of a weakly warped disk with $\beta_{\rm out} = 0.033$. The solid-colored curves show the surface density $\Sigma$ (measured using Equation 18), disk orbital inclination angle $\beta$, phase $\gamma$ (Equation 21) and warp amplitude $|\psi|$ (Equations 22) at different times. The dotted curves shows the linear steady-state solution based on real-time $\Sigma$ and $\epsilon$ profile.

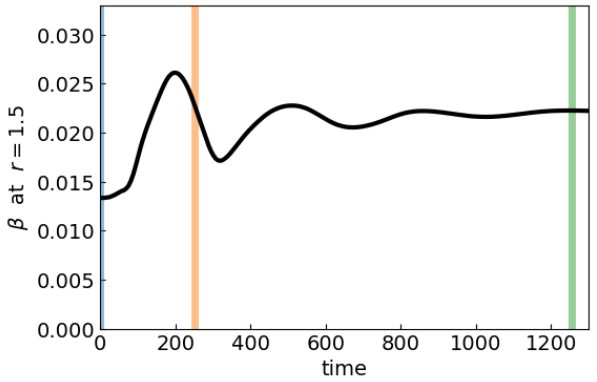


**Figure 4.** Time evolution the disk inclination $\beta$ at $r = 1.5$ in the simulation shown in Figure 3 (C03init, $\beta_{\rm out} = 0.033$). The colored vertical lines mark the time of the snapshots shown in Figure 3.

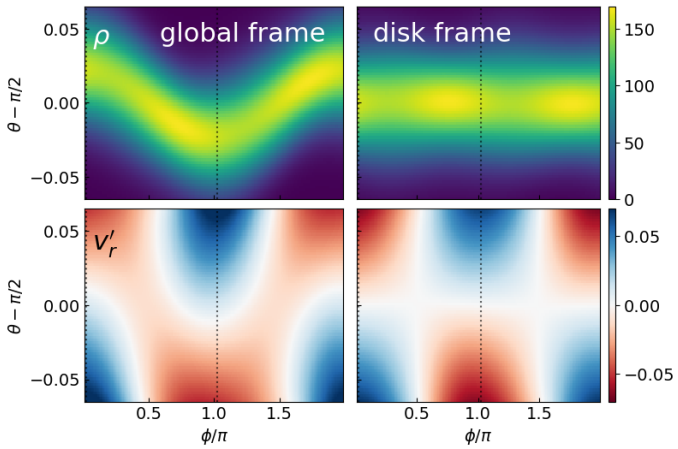


**Figure 5.** Density (top row) and velocity field (bottom row, shown as $v_r' = v_r - \langle v_r \rangle$ with $\langle v_r \rangle$ being the shell average of $v_r$) at $r = 1.5$ for the C03init simulation at $t = 251.2$. The left panels show the quantities in the simulation coordinates, while the right panels show the same data transformed into the local disk frame where the disk midplane is placed at $\theta = \pi/2$. Specifically, we plot on the right the fields of $\rho(\boldsymbol{r}')$ and $v_r(\boldsymbol{r}')$ with $\boldsymbol{r}' = R_y(\beta)R_z(\gamma)\boldsymbol{r}$, where $\boldsymbol{r}$ is the position vector in the unrotated simulation frame and $R_y$ and $R_z$ are the rotational matrices around the $\hat{\boldsymbol{y}}$ and $\hat{\boldsymbol{z}}$ axis. The vertical dotted lines mark the $\phi$ angle where $\pm\boldsymbol{\psi}$ is pointing.

### 3.3. *Vertical and Azimuthal Structures: $\rho$ and $v_r$*

Figure 5 shows the density and radial velocity fields on a spherical shell in the middle of the gap ($r = 1.5$), at time $t = 251.2$. The left panels show those fields as a function of the angular variables used in the Athena++ simulation, i.e., in the global frame in which the inner disk has zero inclination. Because the disk has non-zero inclination at $r = 1.5$, the fields are dominated by a half-sinusoidal variation in $\phi$, i.e., they are proportional to $\cos(m\phi)$ with $m = 1$. To remove that trivial variation, in the right panel, we rotate the coordinate system to one in which $\hat{\boldsymbol{l}}$ is vertical, as detailed in the caption. The rotated $\rho$ is nearly the same as an unperturbed flat disk. But there is a faint hint of an $m = 2$ pattern, due to nonlinear bouncing (Section 4.2). The rotated radial velocity field exhibits the key linear effect: sloshing. As described above, sloshing is driven by the warp; see Equation (7), in which $U_r$ represents sloshing and $RdW/dR$ the warp. In the lower-right panel of Figure 5 we show a vertical line labelled $\angle\psi$ that marks the direction of the warp vector $\boldsymbol{\psi}$. Note that $\boldsymbol{\psi}$ is perpendicular to $\hat{\boldsymbol{l}}$, and so lies in the horizontal direction in the disk frame. As shown by Equation (7), the phase of $U_r$ is

the same as that of the warp when $|\epsilon| \ll 2\alpha$. This is confirmed by Figure 5, where $\angle\psi$ is nearly the same as the peak in radial velocity, because $\epsilon$ is negligibly small in the middle of the gap.

### 3.4. *Internal Torque and Sloshing:* $\boldsymbol{G}$ *and* $\boldsymbol{U_r}$

We define the torque at radius $r$ as the angular momentum flux through a shell of radius $r$, with an extra prefactor of $1/(2\pi)$:

$$\boldsymbol{G} \equiv \frac{r^2}{2\pi}\int_0^{2\pi}\int_0^{\pi} \rho v_r \boldsymbol{r}\times\boldsymbol{v}\ \sin\theta d\theta d\phi\ . \tag{25}$$

Appendix B.3 shows that, in the linear model, one finds

$$\boldsymbol{G} \approx -\frac{1}{2}\Sigma H R^3\Omega^2\left[\mathrm{Re}(U_r), \mathrm{Im}(U_r), 0\right] \tag{26}$$

by inserting parameterization in Equation (10) into the right-hand side of Equation (25). Note that the linear-model torque given by Equation (26) is solely due to sloshing and lies purely in the disk plane. This is not true in general when $v_r$ is not exactly as given by Equation (10): in particular, viscous accretion contributes an extra component in $\boldsymbol{G}$ that is $\propto \hat{\boldsymbol{l}}$.

We define the sloshing vector $\boldsymbol{U}_r$ as the through the in-plane component of $\boldsymbol{G}$ as

$$\boldsymbol{U}_r \equiv -\frac{2}{\Sigma H R^3\Omega^2}\left[\boldsymbol{G} - \left(\boldsymbol{G}\cdot\hat{\boldsymbol{l}}\right)\hat{\boldsymbol{l}}\right]. \tag{27}$$

The direction of $\boldsymbol{U_r}$ within the disk plane is, to linear order in $\psi$, where the radial velocity $v_r$ hits its maximum above the plane (e.g., at $\phi \approx \pi$ in the lower-right panel of Figure 5). The newly introduced vectors $\boldsymbol{G}$ and $\boldsymbol{U_r}$ are related to their complex-valued partners via

$$G \approx \boldsymbol{G}_x + i\boldsymbol{G}_y \tag{28}$$

$$U_r \approx \boldsymbol{U}_{r,x} + i\boldsymbol{U}_{r,y}\ , \tag{29}$$

where the approximation is for small $\beta$.

The vectorial $\boldsymbol{G}$ and $\boldsymbol{U}_r$ can be used to generalize the theory Equations (6) and (7) into nonlinear regime. The disk angular momentum equations exactly implies that $\partial_t \boldsymbol{L}/(2\pi) + \partial_r \boldsymbol{G} = \boldsymbol{T}_{\rm vis}$, where $\boldsymbol{T}_{\rm vis}$ represents viscous torque. In a (quasi-)steady disk,

$$\partial_r \boldsymbol{G} = \boldsymbol{T}_{\rm vis} \tag{30}$$

as the total $\boldsymbol{L}$ only evolves on the viscous timescale.

Observing the second linear (Equation 7, a.k.a. the sloshing equation), we have

$$U_r = \frac{h}{2\alpha + i\epsilon}\psi\ . \tag{31}$$

This relation can be turned into

$$\boldsymbol{U}_r = Q_2\boldsymbol{\psi} + Q_3\hat{\boldsymbol{l}}\times\boldsymbol{\psi} \tag{32}$$

using our vectorial definitions of $U_r$ and $\psi$, where $Q_2$ and $Q_3$ are real numbers. In the linear case,

$$Q_2 = Q_{2,\rm lin} \equiv \mathrm{Re}\left(\frac{h}{2\alpha+i\epsilon}\right) \tag{33}$$

$$Q_3 = Q_{3,\rm lin} \equiv \mathrm{Im}\left(\frac{h}{2\alpha+i\epsilon}\right)\ . \tag{34}$$

We may continue to use Equation (32) in the nonlinear case by having $Q_2$ and $Q_3$ become functions of $\boldsymbol{\psi}$. The theory for how to calculate the nonlinear $Q_2$ and $Q_3$ is worked out in Ogilvie (1999) and Ogilvie & Latter (2013a). We shall discuss their predictions in more detail in Section 4.

The upper row of Figure 6 shows the measured $\boldsymbol{G}$ at $t = 251.2$ and 1256. While the $\boldsymbol{G}\cdot\hat{\boldsymbol{z}}$ component of the torque is mainly from the viscous accretion, the in-plane component of $\boldsymbol{G}$ is generated by the sloshing motion as in Equations (26). We see that the $\hat{x}$ and $\hat{y}$ components of $\boldsymbol{G}$ are evolving toward constant profiles as the linear steady-state condition predicts.

We further measure $\boldsymbol{U}_r$ from our simulations using Equation (27) and evaluate its component from Equation (32). The lower panel of Figure 6 shows that the simulated $\boldsymbol{U}_r$ agrees well with the linear predictions.

## 4. NONLINEAR REGIME

Now we perform a suite of simulations with $\beta_{\rm out}$ between 0.1 and 0.3 (C10 to C30 in Table 1) to explore the nonlinear effects. We set up the disk's initial inclination ($\beta$ and $\gamma$) and sloshing velocity ($\boldsymbol{U}_r$) using their linear steady-state solutions. Although this initial condition no longer represents the exact steady structure when the linear theory breaks down due to large warp amplitudes, it allows the disks to quickly reach a quasi-steady state for us to analyze. Figure 7 shows the time evolution of $\Sigma$, $\beta$ and $|\boldsymbol{\psi}|$ at $r = 1.5$: all three measurements have become quasi-stable in $t \sim 50$ after the initial transient fade away; the density gap is viscously filled in, leading to the slow long-term evolution.

Figure 8 shows the density field from the simulations at $t = 125.6$, with the top and bottom rows being the cross sections at $\theta = \pi/2$ and $\phi = 0$. All disks maintain continuous warped structures when viewed from the side. At the inner midplane disks are nearly circular, but two spiral arms appear at where the disks begin to tilt.

Figure 9 shows the radial profiles of the disks at $t = 125.6$, overplotted with their initial conditions representing the linear predictions of the steady-state solutions. As $\beta_{\rm out}$ raises, the warp amplitude $|\boldsymbol{\psi}|$ increasing

DRAFT

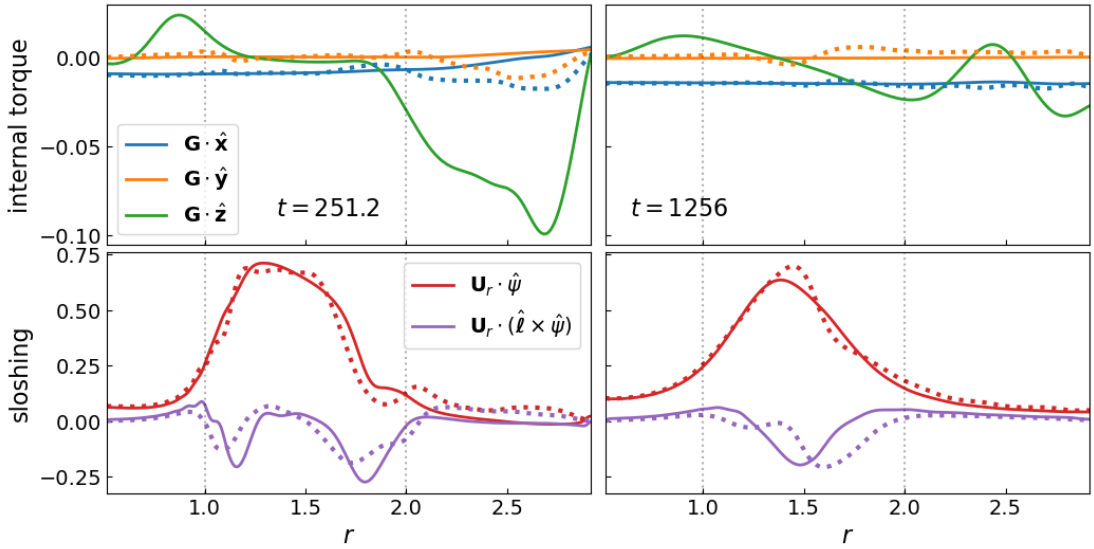


**Figure 6.** Internal torque $\boldsymbol{G}$ and the sloshing vector $\boldsymbol{U}_r$ in the C03init simulation. The upper panel shows the $\hat{\boldsymbol{x}}$-$\hat{\boldsymbol{y}}$-$\hat{\boldsymbol{z}}$ components of $\boldsymbol{G}$ (Equation 25). The lower panel shows the two components of $\boldsymbol{U}_r$ (Equation 27). The dotted curves shows the linear theory predictions (Equations 26, and 31 to 34) based on real-time $\Sigma$ and $\epsilon$ profile.

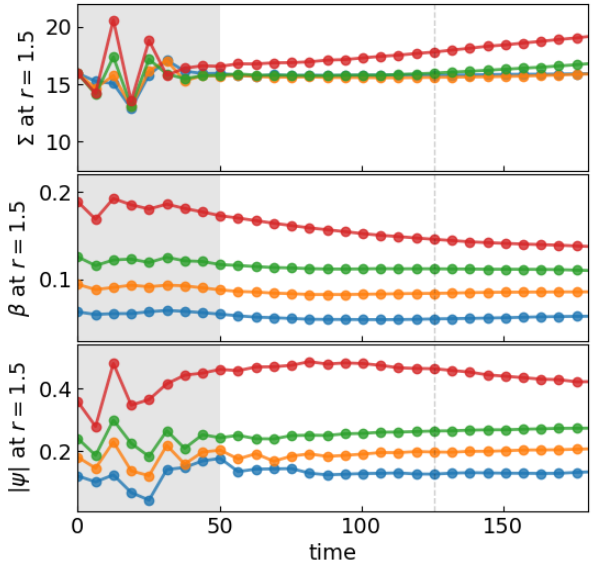


**Figure 7.** Time evolution the disk density $\Sigma$, inclination $\beta$ and warp amplitude $|\boldsymbol{\psi}|$ at $r = 1.5$ in the simulations with $\beta_{\rm out}$ from 0.1 to 0.3 (C10 to C30 in Table 1). The shaded regions represents the first $t \sim 50$ when the disks adjust from initial transient to quasi-steady states. The vertical dashed lines mark $t = 125.6$, at which we analyze the simulation snapshots in later Figures.

accordingly. Except for the $\beta_{\rm out} = 0.3$ case, the linear theory are still able to roughly predicts the $\beta$ and $\boldsymbol{\psi}$ structure. However, we will analyze below several nonlinear effects that the linear theory fails to capture.

### 4.1. *Saturation of Internal Torque*

An important nonlinear effect is the saturation of the disk's internal torque $\boldsymbol{G}$. In the linear theory, both $G$ and $U_r$ are linearly proportional to the warp $\psi$. However, in the *nonlinear* regime, sloshing velocity $\boldsymbol{U}_r$ can max out as $|\boldsymbol{\psi}|$ increases, limiting the amplitude of $\boldsymbol{G}$ that the disk can attain. This saturation process are seen in our nonlinear simulations as we shown in Figures 10 and 11.

Figure 10 shows the measured $|\boldsymbol{U}_r|$ profiles at $t = 125.6$ from the simulations, where we see that the amplitude of $|\boldsymbol{U}_r|$ changes with on $\beta_{\rm out}$ nonlinearly. In particular, the peak values from the $\beta_{\rm out} = 0.2$ (green) and the $\beta_{\rm out} = 0.3$ (red) cases are nearly identical, indicating a saturation of the sloshing amplitude and the internal torque.

This nonlinear effect has been explored semi-analytically by Ogilvie & Latter (2013a) using a local shearing box model. Based on our real-time $\psi$ profile, we solve their Equations (74) to (78) to get a prediction for the local fluid motions, and then use their Equation (92) to get a theoretical prediction for $|\boldsymbol{U}_r|$ (which is denoted as $|Q_4\psi|$ in their paper). The results of the nonlinear predictions are displayed in Figure 10 as faint lines, which are in good agreement with the simulation results.

Figure 11 shows the relation between $|\boldsymbol{U}_r|$ and $|\boldsymbol{\psi}|$. We first calculate the predicted $|\boldsymbol{U}_r|$-vs-$|\boldsymbol{\psi}|$ relation assuming $\alpha = 0.019$ and $\epsilon = 0$. The linear theory prediction is introduced in Section 3.4, which we plot as the gray line. The nonlinear prediction is calculated using Ogilvie & Latter (2013a)'s model and shown as the solid curve. We see the nonlinear prediction saturates

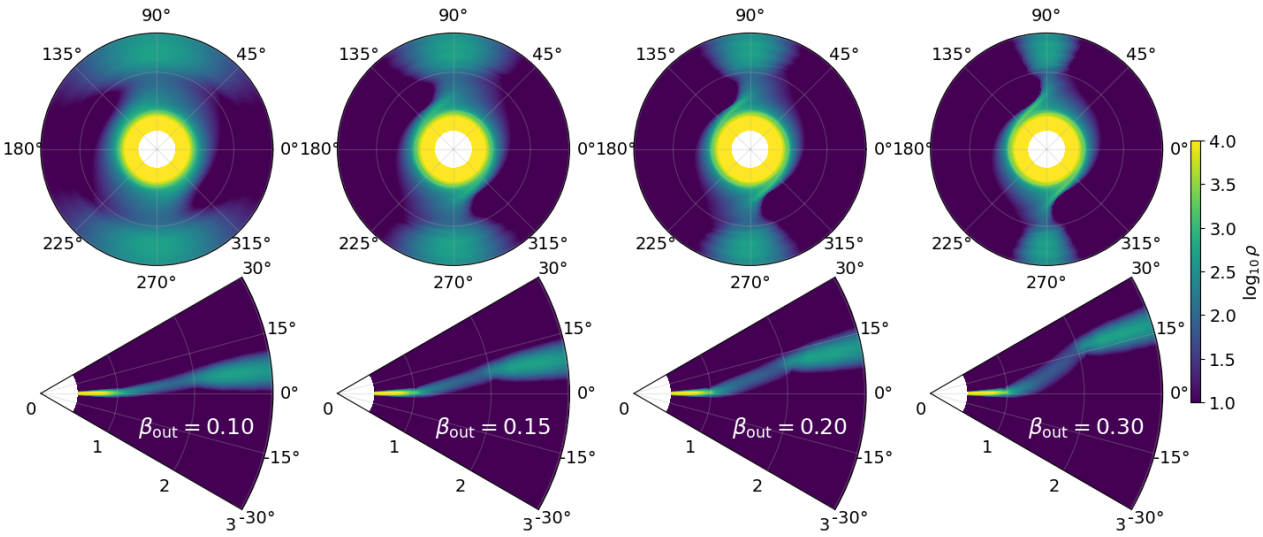


**Figure 8.** Snapshots of the volume density $\rho$ at $t = 125.6$ for simulations in the nonlinear regime. The top and bottom row shows the cross-section at $\theta = \pi/2$ and $\phi = 0$, respectively. From left to right, the columns are from simulations with higher $\beta_{\rm out}$ values.

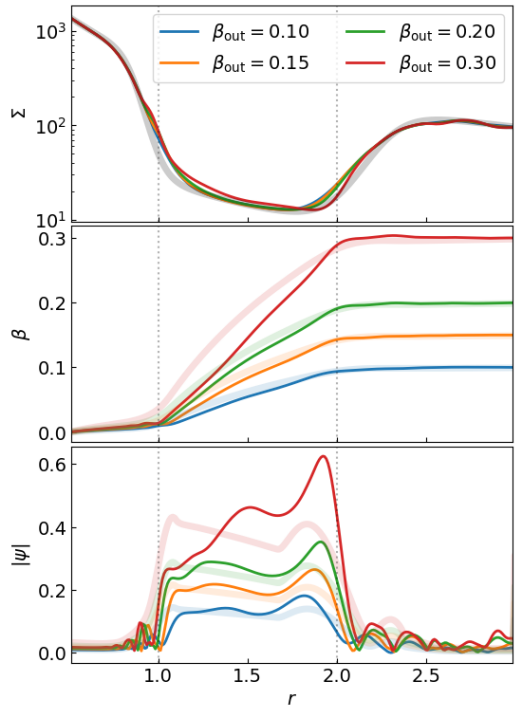


**Figure 9.** Surface density $\Sigma$, inclination profile $\beta$, and warp amplitude $|\psi|$ measured in moderately warped disks with different $\beta_{\rm out}$. The solid lines are the measurements at $t = 125.6$. The faint gray line in the top panel shows the initial density profiles, while the colored faint lines in the other two panels show the linear theory predictions.

at $|\boldsymbol{\psi}| \sim 0.3$ and $|\boldsymbol{U}_r| \approx 2$; at $|\boldsymbol{\psi}| \gtrsim 0.3$, $|\boldsymbol{U}_r|$ starts to deceases with $|\boldsymbol{\psi}|$.

We then measure $|\boldsymbol{U}_r|$ and $|\boldsymbol{\psi}|$ from the simulation snapshots at a few locations inside the density gap and add them into Figure 11. The open circles represent the initial conditions following the linear predictions. The measurements from the $t = 125.6$ snapshots are shown as the solid squares, which all fall down to the nonlinear prediction, indicating a clear trend of saturation.

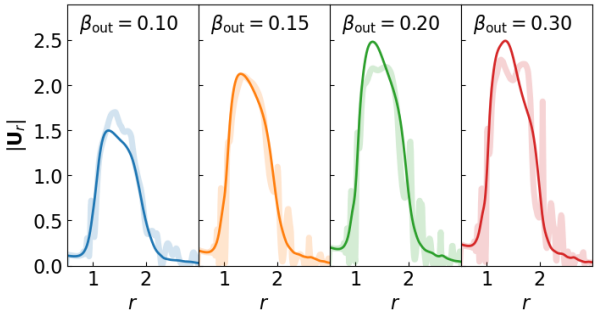


**Figure 10.** Radial profile of $|\boldsymbol{U}_r|$ in simulations with different $\beta_{\rm out}$ (i.e., C10 to C30 in Table 1). The solid lines are the measurement at $t = 125.6$, while the faint lines are predictions based on Ogilvie & Latter (2013a)'s model, using measured $|\boldsymbol{\psi}|$ and $\epsilon$.

### 4.2. *Bouncing Effects*

Figure 12 shows the density of the disks at $r = 1.5$. Stronger bouncing features emerge as $\beta_{\rm out}$ increases, with the density structure showing more extreme vertical compression and expansion along the azimuthal $\hat{\boldsymbol{\phi}}$ direction. We measure the bouncing amplitude through the local scale height $\tilde{H}$ of a disk, which is calculated as the standard deviation of the vertical density distribu-

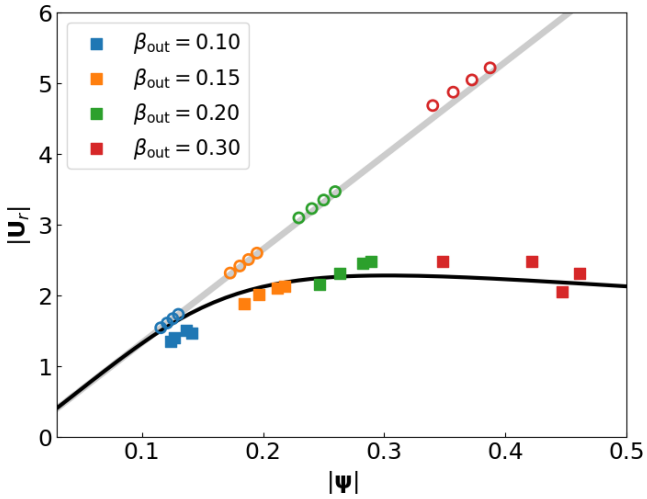


**Figure 11.** Relation between $|\boldsymbol{U}_r|$ and $|\boldsymbol{\psi}|$ in simulations with different $\beta_{\rm out}$ (i.e., C10 to C30 in Table 1). The black line shows the prediction for $\alpha = 0.0189$ and $\epsilon = 0$ based on the shearing-box model in Ogilvie & Latter (2013a), while the faint gray line represents the linear relation. The scattered points show the values for $|\boldsymbol{U}_r|$ and $|\psi|$ measured from the simulations. Each color represents one simulation with a different $\beta_{\rm out}$, while the dots with the same color correspond to the results measured at $r = 1.3$, 1.4, 1.5, and 1.6. The open circles and the solid squares shows the measurement at $t = 0$ and 125.8, respectively.

tion, i.e.,

$$\tilde{H}(r,\phi) = \left[\frac{1}{\Sigma}\int_0^{\pi} \rho\,(\theta_{\rm mid}-\theta)^2\, r^3 d\theta\right]^{1/2}, \qquad (35)$$

where $\theta_{\rm mid}$ is the polar angle of the disk midplane. The measured maximum and minimum of $H$ are shown in the panel for each case. In the most extreme case with $\beta_{\rm out} = 0.3$, the local scale height $\tilde{H}$ bounces between 0.011 and 0.097, while the unperturbed value is $H = 0.037$ at $r = 1.5$.

We use Equations (74) to (78) from Ogilvie & Latter (2013a) to calculate a theoretical predictions for the azimuthal scale height fluctuations using $\alpha = 0.019$, $\epsilon \simeq 0$, and the simulated $|\psi|$. The predicted $\tilde{H}$ are overplotted in Figure 12 as dotted lines, which match the simulation results with remarkable accuracy.

### 4.3. *Surface Density Evolution*

The simulation result also shows different $\Sigma$ evolution for each different $\beta_{\rm out}$ (see the top panel of Figure 9). To quantify this difference, we measure the mass accretion rate,

$$\dot{M}(r) = \int_0^{2\pi}\int_0^{\pi} v_r \rho \sin\theta d\theta d\phi, \qquad (36)$$

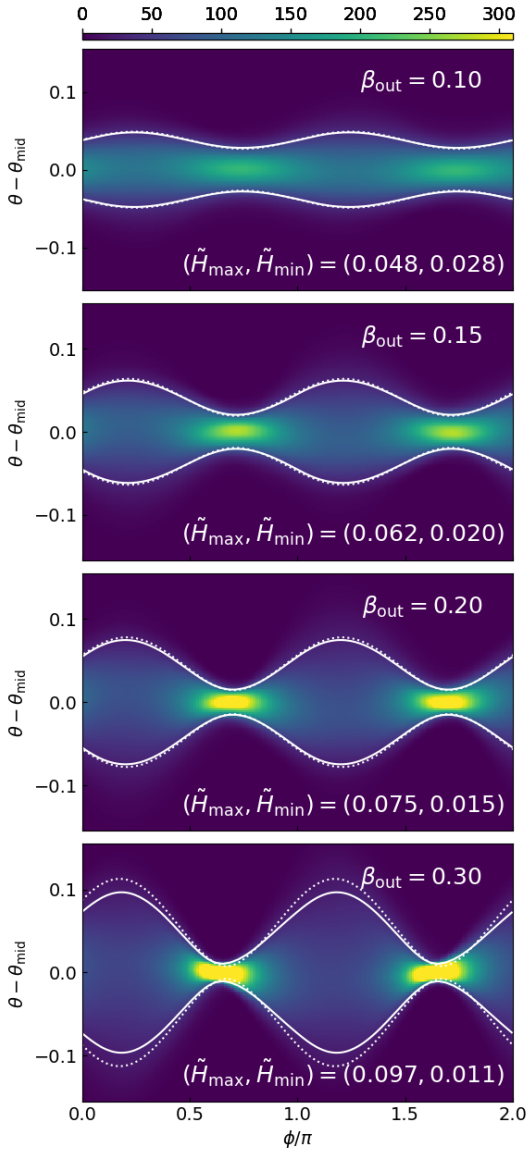


**Figure 12.** Simulated gas density distribution at $r = 1.5$ in four moderately warped disks at $t = 125.6$. The $\theta$ coordinates have been shift to place the disk midplane at the center of the vertical axis. The solid write lines trace the disk scale height measured using Equation (35), while the dotted lines are the predictions based on Ogilvie & Latter (2013a).

inside the density gap (i.e., for $r$ between 1 and 2). The results are shown in Figure 13.

We see that the accretion rate $\dot{M}$ is larger in disks with stronger warp, which is not a surprising result. As we have shown, warp can enhance angular momentum transport across the disk, so the disk density may need to redistribute accordingly by the conservation of total angular momentum. Based on the mass and angular momentum conservation, the predicted accretion rate

DRAFT

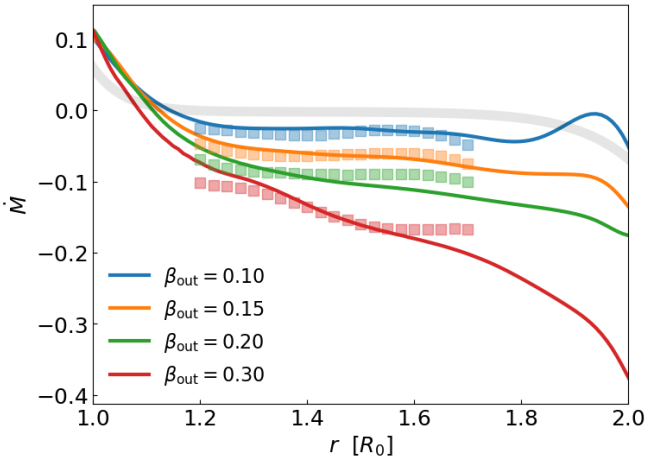


**Figure 13.** Mass flux $\dot{M}$ at the $t = 125.6$. The colored curves show measurements from the simulations using Equation (36), from $r = 1$ to 2. The scattered boxes represent the predictions based on the Equation (37), where we calculated $Q_1$ using the shearing-box model in Ogilvie & Latter (2013a) with the real-time local values of $|\psi|$, $\alpha = 0.019$, $\epsilon \simeq 0$. The faint gray curve corresponds to the theoretical accretion rate if we assume the disk is flat.

$\dot{M}$ of a warped disk is given by (Ogilvie 1999)

$$\dot{M} = \frac{4\pi}{r\Omega}\frac{\partial}{\partial r}\left(Q_1 \Sigma H^2 r^2 \Omega^2\right) - 4\pi Q_2 \Sigma H^2 \Omega \left|\psi\right|^2, \quad (37)$$

where

$$Q_1 = -\frac{1}{\Sigma H^2 \Omega^2 r^2}\boldsymbol{G}\cdot\hat{\boldsymbol{l}} \quad (38)$$

is a dimensionless coefficient that quantifies the $\hat{\boldsymbol{l}}$ component of $\boldsymbol{G}$, and $Q_2$ is the same as defined in Equation (32).

The analytical values of $Q_1$ can be calculated from Equation (91) of Ogilvie & Latter (2013a). We use their model to calculate the analytical prediction of $Q_1$ and $Q_2$ using the real-time local values of $|\psi|$, and then we plug them into Equation (37) with the measured disk profiles to get a semi-analytical prediction for $\dot{M}$. The predicted values of $\dot{M}$ for a range of $r$ are shown in Figure 13 as scattered boxes[4], which are in good agreement with the measured $\dot{M}$.

## 5. DISK BREAKING

As we have seen in the previous section, large warp amplitudes can lead to several nonlinear effects, including torque saturation, bouncing, and modified mass accretion flow. A natural question now is what happens if the warp increases even further? To explore this, we perform an additional simulation with a larger outer inclination angle $\beta_{out} = 0.4$ (i.e., 23°, C40 in Table 1).

### 5.1. *Fiducial Simulation*

Figure 14 shows snapshots of the density field from the simulation; the top and bottom rows show the density distribution in the cross sections at $\theta = \pi/2$ and $\phi = 0$. The disk begins as a continuous warp ($t = 0$), similar to those in the earlier sections, except for the larger warp amplitude. As the system evolves ($t \sim 62.8$ to $\sim 125.6$), however, the inner and outer disk regions gradually detach, forming two disconnected planes separated by a narrow density gap at $r \simeq 1.5R_0$. After falling apart, the two disk portions quickly flatten themselves ($t \sim 188.4$), with the inner and our disks eventually aligned to $\beta_{in} = 0$ and $\beta_{out} = 0.4$, respectively.

Figure 15 illustrates the time evolution of the density, inclination, and warp amplitude profiles during the breaking process. The inclination profile $\beta$ gradually steepen, eventually producing a sharp jump at the breaking point $r \simeq 1.5R_0$. The warp $\psi$ initially spread nearly uniformly between $r = 1$ and $r = 2$; during the evolution, $\psi$ becomes extremely localized, with the maximum $|\psi|$ increasing from $\sim 0.5$ at early times to as high as $\sim 8$ in the final snapshot. While the old density gap is filling up at $r \sim 1$ and $\sim 2$, a new sharp density gap gradually depletes at the breaking radius, where $\Sigma$ decreases by a factor of ten, suggesting that mass flux is significantly enhanced by the strong warp.

We refer to this outcome, where the inner and outer disks detach in terms of $\beta$ and the surface density depletes at the detaching point, as *disk breaking*. This breaking process is spontaneous: there is no explicit external forces tearing the disk, and the gravitational potential is Keplerian. Hence, the breaking arises purely from internal hydrodynamics of the disk.

### 5.2. *Breaking Mechanisms*

What leads the disk to break is the runaway growth of $|\psi|$. To understand that, we consider a set of toy-model time-evolution equations,

$$\Sigma R^2 \Omega \frac{\partial W}{\partial t} = -\frac{1}{R}\frac{\partial G}{\partial R}, \quad (39)$$

$$\frac{\partial G}{\partial t} + \alpha\Omega G = -\alpha \Sigma H^2 \Omega^3 R^2 Q_4 \psi, \quad (40)$$

where the first equation the conservation of angular momentum, the second is a nonlinear time-dependence version of Equation (7) (see Dullemond et al. 2022), and we have set $\epsilon = 0$ and assumed $Q_4$ is mostly real for simplicity.

[4] We assume $\epsilon = 0$ when calculate $Q_1$ and $Q_2$, so we only show the predicted $\dot{M}$ at $r$ far away of the gas edges.

DRAFT

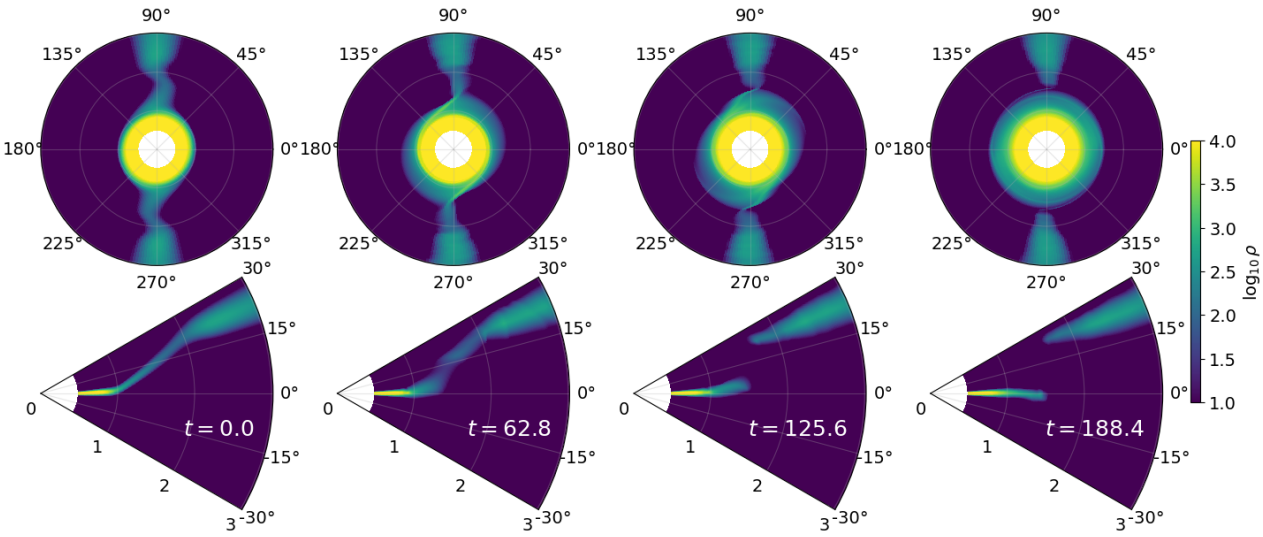


**Figure 14.** Snapshots of the density field $\rho$ from the 'breaking' simulation with $\beta_{\rm out} = 0.40 = 23^\circ$ (i.e., C40 in Table 1). Top and bottom row shows the cross-section at $\theta = \pi/2$ and $\phi = 0$, respectively. The columns represent the time evolution from an initially connected disk ($t = 0.0$) to an eventually broken configuration ($t = 188.4$).

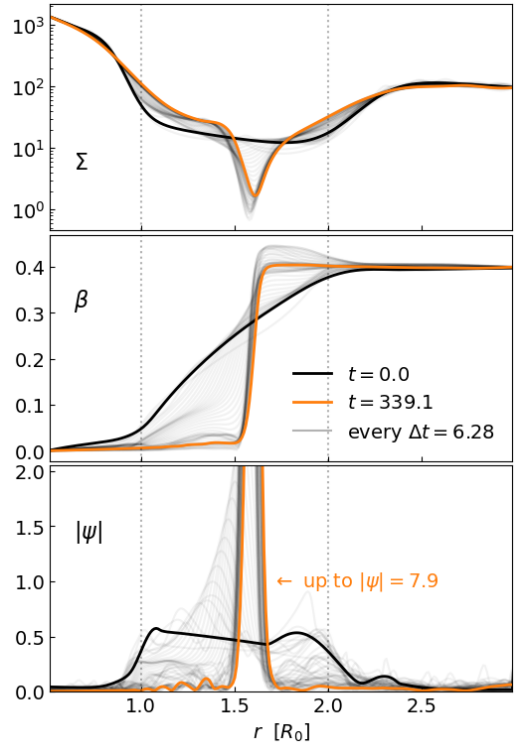


**Figure 15.** Surface density $\Sigma$, inclination profiles $\beta$, and warp amplitude $|\psi|$ measured in the simulaion with $\beta_{\rm out} = 0.4$ (i.e., C40 in Table 1). The black and orange lines are at $t = 0$ and $t = 339.1$, respectively. The faint gray curves shows the time evolution of the profiles at every $\Delta t = 6.28$.

Theories in previous Sections have been focused on the steady-state solution of Equations (39) and (40) with $G = -\Sigma H^2\Omega^2 R^2 Q_4\psi = \text{const}$. However, this solution is unstable against small perturbations when $\partial_\psi\left(Q_4\psi\right) < 0$: We may performing a local stability analysis by assuming $G = G_0 + \delta G$ and $\psi = \psi_0 + \delta\psi$, where $G_0$ and $\psi_0$ are steady-state solutions and $\delta G, \delta\psi \propto e^{\gamma t + ikR}$ are small perturbations. Equations (39) and (40) suggest

$$\gamma\delta G + \alpha\Omega\delta G = -\Sigma H^2\Omega^3 R\partial_\psi\left(Q_4\psi\right)\delta\psi,$$
$$\Sigma R^2\Omega\gamma\delta\psi = k^2\delta G,$$

in the limit of large $k$. Solving for the growth rate $\gamma$ shows that $\gamma > 0$ if $\partial_\psi(Q_4\psi) < 0$. As similar result can be found in Doğan et al. (2018).

This instability condition means, if a local increase in $|\psi|$ reduces the restoring torque, the warp would further amplify through a runaway growth. Consequently, the warp dominates at a particular radius $r_{\rm break}$, around which the inner and outer disk parts are fully misaligned. The resulting large $|\psi|$ at $r_{\rm break}$ would also enhance the local $\dot{M}$ (see Equations 37), leading to a density depletion that disconnects the disk at the point of misalignment.

### 5.3. *Analysis*

The shearing-box model from Ogilvie & Latter (2013a) suggest that the critical warp amplitude for $\partial_\psi(Q_4\psi) < 0$ is about $|\psi|_{\rm crit} = 0.3$. Using the linear solution an estimate (see, e.g., the bottom right panel of Figure 2), our simulation with $\beta_{\rm out} = 0.4$ (C40) would have stead-state $|\psi| \approx 0.5$ and it indeed breaks. Our simulations with $\beta_{\rm out} \leq 0.2$ (C20) would have steadstate $|\psi| \approx 0.25$ and they do not break. These cases are consist with the implication of Ogilvie & Latter (2013a).

However, our simulation with $\beta_{\rm out} = 0.3$ is an exception to the simple breaking theory above. As indicated by the red squares in Figure 11, the simulated warp amplitudes are already above than the critical $|\psi|_{\rm crit}$ for $\partial_\psi(Q_4\psi) < 0$. Yet the disk does not break.

There are a few possible explanation to why this disk does not break. One example is that the instability is suppressed by shock. In a strongly warped (but not yet broken) disk, gas compresses and expands two times per orbit. At sufficiently large amplitude, these compression become supersonically and can produce shocks that damp the warp (Held & Ogilvie 2024; Kaaz et al. 2025), an effect that is not captured in our breaking theory. The disk with $\beta_{\rm out} = 0.3$ in our simulation may be a case when this damping is sufficient to offset the breaking process. Figure 11 shows that the steady state of this disk has $\partial_\psi|Q_4\psi|$ marginally less than zero, so it is possible that the instability is not enough to overcome the dissipation. This shock damping might also contribute to the small discrepancy in two $\tilde{H}$ curves shown in the bottom panel of Figure 12.

Figure 15 shows that, for the disk with $\beta_{\rm out} = 0.4$, the breaking radius is slowly moving outward. The rate of this outward drift appears faster in low-resolution runs. This trend suggests that the migration of the breaking radius at least partially controlled by resolution. A follow-up study may be needed to determine whether this drift is physical or purely numerical.

## 6. CONCLUSION

In this work, we have carried out a systematic investigation of warp steady states (WSS) in accretion disks, spanning the linear, nonlinear, and breaking regimes. Our study combines linear analytic theory, local nonlinear models, and global three-dimensional hydrodynamic simulations. Rather than including an explicit perturber or external torque, we fix the disk inclination angles $\beta_{\rm in}$ and $\beta_{\rm out}$ at the inner and outer boundaries. This setup provides a clean framework for diagnosing how the hydrodynamics of how disks bend, sustain coherent warps, and eventually break, while remaining agnostic about the origin of the warp.

For weakly warped disks, our simulations with $\beta_{\rm out} = 0.033$ confirm the linear theory. We see disks rapidly relaxing to their respective WSS; their simulated warping and inclination profiles, sloshing velocity fields and internal torque fluxes show excellent agreement with the theoretic predictions. Importantly, the predictions remain accurate for real-time steady-state warp profiles even as the background density slowly evolves, implying that protoplanetary disks should stay in quasi-steady warped states on timescales much shorter than their viscous evolution.

As we increase $\beta_{\rm out}$ to inject stronger warps, disks enter the nonlinear regime where several new features emerge. First, the internal torque no longer grows linearly with $|\psi|$, but instead it saturates. Second, the gas exhibits strong "bouncing" motions, undergoing cycles of vertical compression and expansion twice per orbital period; this effect leads to large azimuthal fluctuations in the local disk scale height. Third, large warp $|\psi|$ also enhance the mass accretion flows. All three effects are clearly measured in our simulations and are in good quantitative agreement with the nonlinear predictions (Ogilvie 1999; Ogilvie & Latter 2013a).

When the warp amplitude is increased further, nonlinear disks become unstable and may break. We show in our $\beta_{\rm out} = 0.4$ simulation that a strongly warped disk may undergo a runaway instability: the warp amplitude $|\psi|$ rapidly grows and localizes, and the disk eventually break into two misaligned pieces separated by a density gap. This breaking process occurs spontaneously from internal hydrodynamics, without requiring explicit external forcing. Our analysis suggest that this instability happens when the large warp causes the torque to fully saturate so that $\partial_\psi(Q_4\psi) < 0$; under this condition, local increases in $|\psi|$ reduce the restoring torque, rather than enhancing it. The critical warp amplitude for instability is given by $|\psi|_{\rm crit} \simeq 2\sqrt{\alpha}$ for Keplerian disks.

Overall, our work present a comprehensive picture of the hydrodynamics of warped disks, illustrating how disks may bend, sustain coherent warps, or break. One important topic for future studies is to explore the long-term behavior of broken disks. Some previous simulations have shown examples where disks can heal from breaking and reconnect into whole pieces (e.g., Deng & Ogilvie 2022), but the exact mechanism is not fully understood. Future work may extend our results by incorporating additional physics, such as magnetic fields, turbulence, and gas self-gravity. Explicit perturbers may also be added to further connect our results to more specific astrophysical scenarios. One may also model the observational signatures of the nonlinear behaviors, such as bouncing and enhanced accretion, which may be used for future detections of disk warping.

DRAFT

ACKNOWLEDGMENTS

We thank Nicholas Kaaz, Rixin Li, Alexander Dittmann, Diego Munoz, and Jeremy Rath for their stimulating discussion. Jiaru Li is supported by a CIERA Postdoctoral Fellowship. This work used computing resources provided by Northwestern University and the Center for Interdisciplinary Exploration and Research in Astrophysics (CIERA). This research was supported in part through the computational resources and staff contributions provided for the Quest high performance computing facility at Northwestern University which is jointly supported by the Office of the Provost, the Office for Research, and Northwestern University Information Technology.

DRAFT

# APPENDIX

## A. DERIVATION OF THE LINEAR THEORY

Here we derive the linearized equations of motion for a warp in a globally isothermal protoplanetary disk. The disk is governed by the momentum and continuity equations,

$$(\partial_t + \boldsymbol{v}_{\rm tot}\cdot\boldsymbol{\nabla})\,\boldsymbol{v}_{\rm tot} = -\boldsymbol{\nabla}\Phi - c_s^2\boldsymbol{\nabla}\lambda_{\rm tot}, \tag{A1}$$

$$(\partial_t + \boldsymbol{v}_{\rm tot}\cdot\boldsymbol{\nabla})\,\lambda_{\rm tot} = -\boldsymbol{\nabla}\cdot\boldsymbol{v}_{\rm tot}, \tag{A2}$$

where the subscript "tot" denotes the total value (background + perturbation), $\boldsymbol{v}_{\rm tot}$ is the velocity vector,

$$\lambda_{\rm tot} = \ln\rho_{\rm tot} \tag{A3}$$

is the logarithm of the density, $c_s$ is the globally constant sound speed, and $\Phi$ is the gravitational potential of the central star. We temporarily ignore viscosity.

We shall decompose

$$\lambda_{\rm tot} = \lambda + \lambda' \tag{A4}$$

$$\boldsymbol{v}_{\rm tot} = \boldsymbol{v} + \boldsymbol{v}' \tag{A5}$$

where unsubscripted $\lambda$ and $\boldsymbol{v}$ denote the background, and primed quantities denote the perturbation.

### A.1. *Background*

The background is taken to be axisymmetric and aligned with the vertical axis. In cylindrical coordinates $(R,\phi,z)$, $\boldsymbol{v} = (v_R, v_\phi, v_z) = (0, R\Omega, 0)$. The angular frequency $\Omega(R,z)$ and $\lambda(R,z)$ are related by

$$R\Omega^2 = c_s^2\partial_R\lambda + \partial_R\Phi, \tag{A6}$$

$$0 = c_s^2\partial_z\lambda + \partial_z\Phi \tag{A7}$$

based on Equation (A1).

Taking $\partial_z$(A6) - $\partial_R$(A7) gives $\partial_z\Omega = 0$. Hence, $\Omega$ can be determined by evaluating Equation (A6) at the midplane, which yields

$$\Omega^2 = \Omega_{\rm K}^2 + \frac{c_s^2}{R}\partial_R\lambda_{\rm mid} \tag{A8}$$

where $\Omega_{\rm K} = \Omega_{\rm K}(R)$ is the Keplerian frequency and $\lambda_{\rm mid} = \lambda|_{z=0}$.

Taking $z\times$(A6) - $R\times$(A7) leads to

$$\partial_z \lambda = -\frac{z}{H^2} + \frac{z}{R}\partial_R \lambda, \tag{A9}$$

where

$$H = c_s/\Omega\ . \tag{A10}$$

Near the midplane of the disk, the first term on the right-hand side is dominant over the second as $H^2 \ll R^2$, so $\rho \propto \exp\left\{-z^2/(2H^2)\right\}$. Therefore, the background volume density of the disk has the form

$$\rho(R,z) = \frac{\Sigma}{\sqrt{2\pi}H}\exp\left\{-\frac{z^2}{2H^2}\right\}, \tag{A11}$$

where $\Sigma(R)$ is the radial profile of the disk surface density, which can be chosen freely.

In terms of $\Sigma$, Equation (A8) becomes

$$\Omega^2 = \Omega_{\rm K}^2 + \frac{c_s^2}{R}\partial_R \ln\left(\frac{\Sigma}{H}\right). \tag{A12}$$

We shall also need the epicyclic frequency,

$$\kappa^2 \equiv R^{-3}\partial_R(R^4\Omega^2) \tag{A13}$$

and its deviation from $\Omega$ via

$$\epsilon \equiv \frac{\kappa^2}{\Omega^2} - 1 \tag{A14}$$

$$= R\partial_R \ln(\Omega^2 R^3) \tag{A15}$$

$$\approx R\partial_R\left(\frac{H^2}{R^2}R\partial_R \ln\frac{\Sigma}{H}\right) \tag{A16}$$

where the final expression is to leading order in $H^2/R^2$ when $d_R(\ln\Sigma)$ is order unity.

### A.2. *Perturbation Equations*

Linearizing Equations (A1) and (A2) yields

$$\partial_t v_R' = -\Omega\partial_\phi v_R' + 2\Omega v_\phi' - c_s^2\partial_R\lambda', \tag{A17}$$

$$\partial_t v_\phi' = -\Omega\partial_\phi v_\phi' - (2 + R\partial_R \ln\Omega)\,\Omega v_R' - \frac{c_s^2}{R}\partial_\phi\lambda', \tag{A18}$$

$$\partial_t v_z' = -\Omega\partial_\phi v_z' - c_s^2\partial_z\lambda', \tag{A19}$$

$$\partial_t \lambda' = -\Omega\partial_\phi\lambda' - \frac{1}{R}\partial_R\left(Rv_R'\right) - (\partial_R\lambda)\,v_R' - \frac{1}{R}\partial_\phi v_\phi' - (\partial_z\lambda)\,v_z' - \partial_z v_z', \tag{A20}$$

Following Tanaka et al. (2002) and Ogilvie (2008), we take the azimuthal dependency of linearized variables to be $\propto e^{-i\phi}$, as is appropriate for a warp, and we decompose the vertical dependency in Hermite polynomials. We further simplify by restricting the Hermite expansion to the leading-order contributions, which results in setting

$$\frac{v_R'}{\Omega R} = U_R\frac{z}{H}e^{-i\phi}, \tag{A21}$$

$$\frac{v_\phi'}{\Omega R} = U_\phi\frac{z}{H}e^{-i\phi}, \tag{A22}$$

$$\frac{v_z'}{\Omega R} = U_z e^{-i\phi}, \tag{A23}$$

$$\lambda' = \Lambda\frac{z}{H}e^{-i\phi}, \tag{A24}$$

DRAFT

where $U_R$, $U_\phi$, $U_z$, and $\Lambda$ are complex coefficients that depend on $R$ and $t$. Plugging these into Equations (A17) to (A20) gives the evolution equations

$$\Omega^{-1}\partial_t U_R = iU_R + 2U_\phi + h^2 R(\partial_R \ln H)\Lambda - h^2 R\partial_R \Lambda, \tag{A25}$$

$$\Omega^{-1}\partial_t U_\phi = iU_\phi - (2 + R\partial_R \ln \Omega)\, U_R + ih^2\Lambda, \tag{A26}$$

$$\Omega^{-1}\partial_t U_z = iU_z - h\Lambda, \tag{A27}$$

$$\Omega^{-1}\partial_t \Lambda = i\Lambda - R\partial_R \ln\left(\Omega\Sigma H R^2\right) U_R - R\partial_R U_R + iU_\phi + \frac{1}{h}U_z - hR\partial_R \ln\left(\Sigma H^2\right) U_z, \tag{A28}$$

where

$$h = H/R \tag{A29}$$

is the aspect ratio. To derive Equation (A28), we use Equations (A9) and (A11) to calculate $\partial_z\lambda$ and $\partial_R\lambda$, respectively. In addition, although the factors of $z$ cancel from the first three equations, some of the terms in Equation (A28) have coefficient $z$, and others have coefficient $z^3$. Since we are really extracting the projection of this equation onto the first Hermite polynomial, we replace those coefficients by their projections, which amounts to replacing $z \to H$ and $z^3 \to 3H^3$.

### A.3. *Steady-State Equations*

Henceforth, we consider steady-state equations ($\partial_t \to 0$). Equation (A27) gives $\Lambda = iU_z/h$, which can be used to eliminate $\Lambda$ in other three equations. We then eliminate $U_\phi$ by forming two different combinations of the three equations: $-i\times$(A25)$+2\times$(A26) and $-i\times$(A25)$+$(A26)$+$(A28). These combinations gives

$$0 = \frac{d}{dR}\left[\Sigma H\Omega^2 R^3 \left(U_R + hU_z\right)\right], \tag{A30}$$

$$0 = \frac{d\ln\left(\Omega^2 R^3\right)}{dR}\left(U_R + hU_z\right) + h\frac{d}{dR}U_z, \tag{A31}$$

which are two equations for two unknowns: $U_R + hU_z$ and $U_z$. The former is related to the radial speed in the (spherical) $\hat{\boldsymbol{r}}$ direction, $v_r' = (R/r)v_R' + (z/r)v_z'$, which implies

$$\frac{v_r'}{\Omega R} \approx \left(U_R + hU_z\right)\frac{z}{H}e^{-i\phi} \tag{A32}$$

after dropping the $O(z^2/r^2)$ correction. We therefore define

$$U_r \equiv U_R + hU_z \tag{A33}$$

which represents the amplitude of $v_r'$. Equations (A30–A31) then become

$$0 = \frac{d}{dR}\left(\Sigma H\Omega^2 R^3 U_r\right), \tag{A34}$$

$$0 = \epsilon U_r + hR\frac{d}{dR}U_z. \tag{A35}$$

We will show in A.4 that viscosity contributes an extra $-2i\alpha U_r$ term to the right-hand-side of Equation (A35).

Equations (6) and (7) then follow after defining

$$W \equiv -iU_z \tag{A36}$$

and including the viscous term.

### A.4. *Viscous Terms*

Here, we derive the viscous term we added in the last step of the previous section. We take the viscous force per unit mass to be

$$\boldsymbol{f}_{\rm tot} = \frac{1}{R\Omega^2\rho_{\rm tot}}\boldsymbol{\nabla}\cdot\left(\nu\rho_{\rm tot}\boldsymbol{\tau}_{\rm tot}\right), \tag{A37}$$

DRAFT

where $\boldsymbol{\tau}$ is the stress tensor and $\nu$ is the kinematic viscosity,

$$\nu = \alpha c_s H, \tag{A38}$$

with $\alpha$ being the viscosity parameter as in the Shakura & Sunyaev (1973) model. This $\boldsymbol{f}_{\rm tot}$ is to be added to the right-hand side of Equation (A1).

We derive the perturbed $\boldsymbol{f}'$, which is to be inserted on the right-hand-side of the steady-state versions of Equations (A17)–(A19) by first working in the zero-inclination frame, where $v_z' = 0$. We shall then rotate to obtain the general form. Anticipating that the vertical viscous force is small, Equation (A19) implies $\lambda' = 0$. Then,

$$\boldsymbol{f}' = \frac{1}{R\Omega^2\rho}\boldsymbol{\nabla}\cdot(\nu\rho\boldsymbol{\tau}'). \tag{A39}$$

The most important terms in $\boldsymbol{\tau}'$ are

$$\tau_{Rz}' = \tau_{zR}' = \partial_z v_R', \tag{A40}$$
$$\tau_{\phi z}' = \tau_{z\phi}' = \partial_z v_\phi', \tag{A41}$$

as the main effect of viscosity is to act on the sloshing-induced vertical shear in the horizontal velocity components (see also Papaloizou & Lin 1995). Hence,

$$\boldsymbol{f}' \simeq \frac{1}{R\Omega^2\rho}\frac{\partial}{\partial z}\left[\nu\rho\left(\hat{\boldsymbol{R}}\partial_z v_R' + \hat{\boldsymbol{\phi}}\partial_z v_\phi'\right)\right] \tag{A42}$$
$$\simeq -\frac{\alpha z}{R\Omega}\left[\left(\partial_z v_R'\right)\hat{\boldsymbol{R}} + \left(\partial_z v_\phi'\right)\hat{\boldsymbol{\phi}}\right] \tag{A43}$$
$$\simeq -\frac{\alpha v_R'}{R\Omega}\left[\hat{\boldsymbol{R}} + \left(\frac{i}{2}\right)\hat{\boldsymbol{\phi}}\right], \tag{A44}$$

where we keep leading order terms by assuming $\partial_R, \partial_\phi \to \mathcal{O}(1)$ and $\partial_z \to \mathcal{O}(1/h)$ (see also Papaloizou & Lin 1995), and in the third equality we eliminate $v_\phi'$ by using the dominant contribution from Equation (A17).

In order to rotate $\boldsymbol{f}'$, we simply replace $v_R' \to v_r'$; other contributions to the rotation are higher order. The result is that Equations (A25)–(A26) are to be modified by adding to their respective right-hand-sides $-\alpha U_r$ and $\frac{1}{2}i\alpha U_r$. Finally, when we carry through the manipulations described in Section A.3, the viscous force adds $-2i\alpha U_r$ to the right-hand side of Equation (A35). It also adds a term to Equation (A34), but one that is smaller than the other in Equation (A34) term by $\mathcal{O}(\alpha)$, and so we drop it. Our viscous term is the same as those in Papaloizou & Lin (1995) and Lubow & Ogilvie (2000), except that their terms are proportional to $U_R$.

## B. MEASUREMENT OF DISK STATES IN SIMULATIONS

The linear theory in the main text adopts complex-number notations, while the simulations are performed in real-valued space using 3D spherical frame. This Appendix shows how to related complex linear quantities and the simulation measurement.

### B.1. *An Useful Preparation*

Most of our profile measurements adopt the general form

$$F = \iint_S f(\boldsymbol{s})dS = r^2\int_0^{2\pi}\int_0^{\pi} f(\boldsymbol{s})d\theta d\phi, \tag{B45}$$

where $S$ is a spherical shell of radius $r$ and $\boldsymbol{s}$ are points on this shell. We may also parametrize this integral using cylindrical $(z,\phi)$ as

$$F = r\int_0^{2\pi}\int_{-r}^{+r} f(\boldsymbol{s})dzd\phi, \tag{B46}$$

where $\boldsymbol{s} = \sqrt{r^2-z^2}\hat{\boldsymbol{R}} + z\hat{\boldsymbol{z}}$.

DRAFT

Now we will apply approximations to match the formalism we used for the linear theory. Instead of integrating over $S$, we want to integrate area into a cylinder defined by $\boldsymbol{r} = r\hat{\boldsymbol{R}} + z\hat{\boldsymbol{z}}$. Assuming that $f$ is only significant near the midplane of the disk at $z = r\sin\beta$, we have

$$f(\boldsymbol{s}) = f(\boldsymbol{r})\left[1 + \mathcal{O}\left(\beta^2 \frac{\partial \ln f}{\partial \ln r}\right)\right], \tag{B47}$$

in the limit of $\beta$ is small. Hence, we can say that

$$F \simeq r\int_0^{2\pi}\int_{-\infty}^{+\infty} f(\boldsymbol{r}) dz d\phi \tag{B48}$$

with a $\mathcal{O}(\beta^2)$ correction factor.

### B.2. *Tilt Vector $\hat{\boldsymbol{l}}$ and Complex W*

The tilt vector is defined as $\hat{\boldsymbol{l}} = \boldsymbol{L}/|\boldsymbol{L}|$, where $\boldsymbol{L}$ is the total orbital angular momentum vector. We measure $\boldsymbol{L}$ from our simulation as

$$\begin{aligned}\boldsymbol{L}(r) =& r^2\int_0^{2\pi}\int_0^{\pi} \rho_{\rm tot}\boldsymbol{r}_{\rm tot}\times\boldsymbol{v}_{\rm tot}\sin\theta d\theta d\phi &\text{(B49)}\\ \simeq& r\int_0^{2\pi}\int_{-\infty}^{+\infty}(\rho+\rho')\left(R\hat{\boldsymbol{R}} + z\hat{\boldsymbol{z}}\right)\times\left(v'_R\hat{\boldsymbol{R}} + \Omega R\hat{\boldsymbol{\phi}} + v'_\phi\hat{\boldsymbol{\phi}} + v'_z\hat{\boldsymbol{z}}\right) dz d\phi &\text{(B50)}\end{aligned}$$

where we have expanded the total fluid quantities into the background and the perturbation as in Equation (A4) in the second line, and we also switch to the cylindrical coordinates as used in Section 2.

In the *linear* model, we have

$$\boldsymbol{L}(r) \simeq \Omega R^3\int_0^{2\pi}\int_{-\infty}^{+\infty}\left[\hat{\boldsymbol{z}} - \frac{v'_z}{\Omega R}\hat{\boldsymbol{\phi}} + \frac{z}{R}\frac{v'_R}{\Omega R}\hat{\boldsymbol{\phi}} - \frac{z}{R}\frac{v'_\phi}{\Omega R}\hat{\boldsymbol{R}} - \lambda'\frac{z}{R}\hat{\boldsymbol{R}}\right]\rho dz d\phi, \tag{B51}$$

where we have set $r = R$, dropped the nonlinear terms, dropped terms that are antisymmetric in $z$ based on Equations (A21) to (A24). To related vector $\boldsymbol{L}$ to complex numbers, we consider the cartesian components

$$\begin{aligned}\hat{\boldsymbol{x}}\cdot\boldsymbol{L} \simeq& \Omega R^3\int_0^{2\pi}\int_{-\infty}^{+\infty}\left[\left(\frac{v'_z}{\Omega R} - \frac{z}{R}\frac{v'_R}{\Omega R}\right)\sin\phi - \left(\frac{z}{R}\frac{v'_\phi}{\Omega R} + \lambda'\frac{z}{R}\right)\cos\phi\right]\rho dz d\phi, &\text{(B52)}\\ \hat{\boldsymbol{y}}\cdot\boldsymbol{L} \simeq& \Omega R^3\int_0^{2\pi}\int_{-\infty}^{+\infty}\left[\left(-\frac{v'_z}{\Omega R} + \frac{z}{R}\frac{v'_R}{\Omega R}\right)\cos\phi - \left(\frac{z}{R}\frac{v'_\phi}{\Omega R} + \lambda'\frac{z}{R}\right)\sin\phi\right]\rho dz d\phi, &\text{(B53)}\\ \hat{\boldsymbol{z}}\cdot\boldsymbol{L} \simeq& \Omega R^3\int_0^{2\pi}\int_{-\infty}^{+\infty}\hat{\boldsymbol{z}}\rho dz d\phi = 2\pi\Sigma\Omega R^3. &\text{(B54)}\end{aligned}$$

Inserting the real parts of Equations (A21) to (A24) into Equations (B55) and (B56), we can perform the $\phi$ integral and get

$$\begin{aligned}\hat{\boldsymbol{x}}\cdot\boldsymbol{L} \simeq& \pi\Omega R^3\int_{-\infty}^{+\infty}\left[\mathrm{Im}\left(U_z - h\frac{z^2}{H^2}U_R\right) - \mathrm{Re}\left(h\frac{z^2}{H^2}U_\phi + h\frac{z^2}{H^2}\Lambda\right)\right]\rho dz, &\text{(B55)}\\ \hat{\boldsymbol{y}}\cdot\boldsymbol{L} \simeq& \pi\Omega R^3\int_{-\infty}^{+\infty}\left[\mathrm{Re}\left(-U_z + h\frac{z^2}{H^2}U_R\right) - \mathrm{Im}\left(h\frac{z^2}{H^2}U_\phi + h\frac{z^2}{H^2}\Lambda\right)\right]\rho dz. &\text{(B56)}\end{aligned}$$

Using the relation that

$$\int_{-\infty}^{+\infty}\rho dz = \int_{-\infty}^{+\infty}\rho\frac{z^2}{H^2}dz = \Sigma, \tag{B57}$$

we have

$$\begin{aligned}\hat{\boldsymbol{x}}\cdot\boldsymbol{L} \simeq& \pi\Sigma\Omega R^3\left[\mathrm{Im}\left(U_z - hU_R\right) - \mathrm{Re}\left(hU_\phi + h\Lambda\right)\right], &\text{(B58)}\\ \hat{\boldsymbol{y}}\cdot\boldsymbol{L} \simeq& \pi\Sigma\Omega R^3\left[\mathrm{Re}\left(-U_z + hU_R\right) - \mathrm{Im}\left(hU_\phi + h\Lambda\right)\right], &\text{(B59)}\\ \hat{\boldsymbol{z}}\cdot\boldsymbol{L} \simeq& 2\pi\Sigma\Omega R^3. &\text{(B60)}\end{aligned}$$

DRAFT

Note that

$$(\hat{\boldsymbol{x}} + i\hat{\boldsymbol{y}}) \cdot L \simeq \pi\Sigma\Omega R^3 \left(-iU_z + ihU_R - hU_\phi - h\Lambda\right), \tag{B61}$$
$$= 2\pi\Sigma\Omega R^3 \left[-iU_z + \mathcal{O}(hU_r + hU_\phi)\right], \tag{B62}$$

where the second line holds when the disk is in a steady state so that $\Lambda = iU_z/h$ (Equation A27) Also from the steady-state relations (e.g., Equation 7), we have

$$\mathcal{O}(hU_R) = \mathcal{O}(hU_\phi) = \mathcal{O}(hU_r) = \mathcal{O}\left(\frac{h^2}{2\alpha + i\epsilon}\psi\right) \ll |U_z|, \tag{B63}$$

where inequality holds if $\psi$ is small and when $h \lesssim |2\alpha + i\epsilon|$ (i.e., when non-resonant). By setting $W = -iU_z$, we get

$$\boldsymbol{L} \simeq 2\pi\Sigma\Omega R^3 \left[\mathrm{Re}(W), \mathrm{Im}(W), 1\right] \tag{B64}$$

and

$$\hat{\boldsymbol{l}} \simeq \left[\mathrm{Re}(W), \mathrm{Im}(W), 1\right], \tag{B65}$$

which is introduced in Section 2 of the main text, with an order of $\mathcal{O}\left(\frac{h^2}{2\alpha+i\epsilon}\psi\right)$ error. It is then obvious that

$$\boldsymbol{\psi} = \frac{d\boldsymbol{l}}{d\ln r} = \left[\mathrm{Re}(\psi), \mathrm{Im}(\psi), 1\right]. \tag{B66}$$

Hence, the complex numbers $W$ and $\psi$ are

$$W \simeq \hat{\boldsymbol{l}}_x + i\hat{\boldsymbol{l}}_y, \tag{B67}$$
$$\psi \simeq \boldsymbol{\psi}_x + i\boldsymbol{\psi}_y, \tag{B68}$$

where $x$ and $y$ subscripts are the Cartesian components of those vectors, as shown in Section 3.

### B.3. *Torque $\boldsymbol{G}$ and Sloshing $U_r$*

We measure the internal torque $\boldsymbol{G}$ as

$$\boldsymbol{G}(r) = \frac{r^2}{2\pi}\int_0^{2\pi}\int_0^{\pi} (\boldsymbol{r} \times \boldsymbol{v})\, v_r \rho d\theta d\phi. \tag{B69}$$

from the simulations. Similar to what we do for $\boldsymbol{L}$, we have the *linear* approximation for $\boldsymbol{G}$ as

$$\boldsymbol{G} \simeq \frac{R}{2\pi}\int_0^{2\pi}\int_{-\infty}^{+\infty} (\boldsymbol{r} \times \boldsymbol{v})\, v_r' \rho dz d\phi, \tag{B70}$$
$$= \frac{1}{2\pi}\Omega R^3 \int_0^{2\pi}\int_{-\infty}^{+\infty} \left(\hat{\boldsymbol{z}} - \frac{z}{R}\hat{\boldsymbol{R}}\right) v_r' \rho dz d\phi \tag{B71}$$

where the unprimed and primed quantities refer to the background and perturbations. Inserting Equation (10) into (B72), we have

$$\boldsymbol{G} \simeq -\frac{1}{2\pi}\Omega^2 R^4 h \int_0^{2\pi}\int_{-\infty}^{+\infty} \frac{z^2}{R^2}\left[\mathrm{Re}(U_r)\cos^2\phi\hat{\boldsymbol{x}} + \mathrm{Im}(U_r)\sin^2\phi\hat{\boldsymbol{y}}\right]\rho dz d\phi \tag{B72}$$
$$= -\frac{1}{2}\Sigma H R^3 \Omega^2 \left[\mathrm{Re}(U_r), \mathrm{Im}(U_r), 0\right] \tag{B73}$$

which related complex $U_r$ and vector $\boldsymbol{G}$.

DRAFT

## C. DETAILS OF HYDRODYNAMIC SIMULATION SETUP

### C.1. *Grid and Boundary Conditions*

Our simulations are preformed with Athena++ (Stone et al. 2020). We adopt spherical polar coordinates and uniformly spaced grid cells in $r$, $\theta$ and $\phi$ for our simulations. The azimuthal angle $\phi$ ranges from 0 to $2\pi$ while the radial $r$ and polar $\theta$ coverages are given in Table 1. The $\phi$ domain is periodic; at each $r$ and $\theta$ boundary of the domain, two ghost cells are attached outside the active mesh to implement boundary conditions.

The $\theta$ boundaries are placed sufficiently far from the disk midplane ($\geq 10H$ away from at $r = R_0$, $\geq 5.5H$ at $r = 1.5R_0$, and $\geq 2.5H$ at $r = 3.5R_0$) to ensure they do not influence the disk evolution. We impose reflective conditions, which are found to be the best for maintaining the vertical hydrostatic equilibrium of the disk and minimizing spurious inflows or outflows. Specifically, we copy the values of density $\rho$, radial velocity $v_r$, and azimuthal velocity $v_\phi$ from the last active cells into the ghosts, while the polar velocity $v_\theta$ is copied with its sign reversed. Similar boundary conditions have been used in a number of previous studies (e.g., Zhu 2019; Kimmig & Dullemond 2024).

The radial boundary condition needs to achieve two goals: (i) keeping the disk at fixed tilts, and (ii) allowing the sloshing motion to be consistent with the warp-steady-state condition. For (i), we hold the density values in the ghost cells at their initial values, so that the midplane of the disk is fixed. For (ii), we follow Equation (6) to set

$$\frac{v_r}{r\Omega} = U_r \propto \left(\Sigma H R^3 \Omega^2\right) = constant \tag{C74}$$

at the boundary.

In the following, we describe the details of our radial boundary implementation. We denote quantities associated with the first/last active cells with $'$ and those associated with the ghost cells with $''$. The density values in the ghost cells are held at their initial values, i.e.,

$$\rho'' = \rho''(t = 0). \tag{C75}$$

The velocity values in ghost cells are set in three steps: (1) calculate the cylindrical velocity components $(v'_R, v'_\phi, v'_z)$ with $\hat{\boldsymbol{z}}$ pointing at the direction of the disk plane (defined by $\beta = 0$ and $\beta = \beta_{\rm out}$ at the inner and outer boundaries, respectively); (2) calculate these components for the ghost cells as

$$v''_R = v'_R \left(\frac{R''}{R'}\right)^{-1/2}, \tag{C76}$$

$$v''_\phi = v'_\phi \left(\frac{R''}{R'}\right)^{-1/2}, \tag{C77}$$

$$v''_z = 0, \tag{C78}$$

where the factor $-1/2$ is to keep $U_r$ as a constant across the boundary based on Equation (C74); then (3) convert them to the spherical-polar components $(v''_r, v''_\theta, v''_\phi)$ and assign these values to the ghost cells. In short, this method is to set the ghost cell velocity to $\boldsymbol{v}'' = \left[\boldsymbol{v}' - \left(\boldsymbol{v}' \cdot \hat{\boldsymbol{l}}\right)\hat{\boldsymbol{l}}\right] \times (r''/r')^{-1/2}$, where $\hat{\boldsymbol{l}}$ is the target tilt at the boundary.

### C.2. *Initial Condition, tilting, and Time Evolution*

The initial disk is set in two steps: first setting up a disk in its flat background state, and then applying a warp structure by tilting the disk. We use an initial background surface density profile

$$\Sigma(r) = \Sigma_0 r^{-3/2} \frac{1}{f_{\rm gap}(r)}, \tag{C79}$$

where

$$f_{\rm gap}(r) = 1 + \frac{K-1}{2}\left[\tanh\left(\frac{r - R_a}{\Delta_a}\right) - \tanh\left(\frac{r - R_b}{\Delta_b}\right)\right] \tag{C80}$$

controls the shape of the gap. The parameters $R_a$ and $R_b$ are the locations of the inner and outer gap edges, $\Delta_a$ and $\Delta_b$ are the steepness of the edges, and the constant $K$ determines the depth of the gap. We use parameter values

DRAFT

$(R_a,\ R_b,\ \Delta_a,\ \Delta_b,\ K) = (1,\ 2,\ 0.1,\ 0.2,\ 19)$ in all simulations. The background volume density $\rho$ and $\Omega$ are set as in Appendix A.1.

To apply a tilting profile

$$\hat{\boldsymbol{l}} = [\sin(\beta)\cos(\gamma), \sin(\beta)\sin(\gamma), \cos(\beta)]\,, \tag{C81}$$

we rotate the fluid element at $\boldsymbol{r} = (r, \theta, \phi)$ to a new coordinate $\boldsymbol{r}' = (r, \theta', \phi')$ so that

$$\boldsymbol{r}' = \mathbf{R}_z(\gamma)\mathbf{R}_y(\beta)\boldsymbol{r}, \tag{C82}$$

where $\mathbf{R}_z(\gamma)$ and $\mathbf{R}_y(\beta)$ are the standard 3D rotational matrices around the $\hat{\boldsymbol{z}}$ and $\hat{\boldsymbol{y}}$ axes, respectively. When we calculate $\boldsymbol{r}'$, we convert $\boldsymbol{r}$ into cartesian coordinate so that apply $\mathbf{R}_z(\gamma)$ and $\mathbf{R}_y(\beta)$ can be applied; the resulting $\boldsymbol{r}'$ is also in Cartesian coordinates, based on which we get spherical-polar coordinates $(r, \theta', \phi')$. As we rotate a fluid element from $\boldsymbol{r}$ to $\boldsymbol{r}'$, we change its velocity vector to

$$\boldsymbol{v}' = \mathbf{R}_z(\gamma)\mathbf{R}_y(\beta)\boldsymbol{v} \tag{C83}$$

and preserve its density $\rho$.

When we analyze a simulation, we can reverse this tilting procedure using the real-time measured $\beta$ and $\gamma$. This allows us to map from the simulation coordinates $\boldsymbol{r}_{\rm sim}$ to the disk midplane coordiantes $\boldsymbol{r}_{\rm disk}$ via

$$\boldsymbol{r}_{\rm disk} = \mathbf{R}_y(-\beta)\mathbf{R}_z(-\gamma)\boldsymbol{r}_{\rm sim}. \tag{C84}$$

This is how we obtain the disk-plane snapshots in the right panels of Figure 5 and in Figure 12.

Local-Lax-Friedrichs method (LLF) is adopted to solve the hydrodynamic equations in our simulations, where the spatial reconstruction of the primitive fluid quantities is done using the piecewise Linear Method (PLM). We perform time integrations using the second-order accurate Runge-Kutta/Heun's method (RK2). All of the numerical methods here are already implemented in the public version of Athena++.

DRAFT

## REFERENCES


Benisty, M., Juhász, A., Facchini, S., et al. 2018, A&A, 619, A171

Benisty, M., Dominik, C., Follette, K., et al. 2023, in Astronomical Society of the Pacific Conference Series, Vol. 534, Protostars and Planets VII, ed. S. Inutsuka, Y. Aikawa, T. Muto, K. Tomida, & M. Tamura, 605, doi: 10.48550/arXiv.2203.09991

Bohn, A. J., Benisty, M., Perraut, K., et al. 2022, A&A, 658, A183

Casassus, S., Marino, S., Pérez, S., et al. 2015, ApJ, 811, 92

Casassus, S., Avenhaus, H., Pérez, S., et al. 2018, MNRAS, 477, 5104

Deng, H., & Ogilvie, G. I. 2022, MNRAS, 512, 6078

Deng, H., Ogilvie, G. I., & Mayer, L. 2021, MNRAS, 500, 4248

Doğan, S., Nixon, C. J., King, A. R., & Pringle, J. E. 2018, MNRAS, 476, 1519

Dullemond, C. P., Kimmig, C. N., & Zanazzi, J. J. 2022, MNRAS, 511, 2925

Fairbairn, C. W. 2025, ApJ, 979, 156

Fairbairn, C. W., & Ogilvie, G. I. 2021a, MNRAS, 505, 4906

—. 2021b, MNRAS, 508, 2426

Fairbairn, C. W., & Stone, J. M. 2025, arXiv e-prints, arXiv:2506.08839

Foucart, F., & Lai, D. 2014, MNRAS, 445, 1731

Gammie, C. F., Goodman, J., & Ogilvie, G. I. 2000, MNRAS, 318, 1005

Held, L. E., & Ogilvie, G. I. 2024, MNRAS, 535, 3108

Kaaz, N., Liska, M. T. P., Jacquemin-Ide, J., et al. 2023, ApJ, 955, 72

Kaaz, N., Lithwick, Y., Liska, M., & Tchekhovskoy, A. 2025, ApJ, 979, 192

Keppler, M., Penzlin, A., Benisty, M., et al. 2020, A&A, 639, A62
Kimmig, C. N., & Dullemond, C. P. 2024, A&A, 689, A45
Kraus, S., Kreplin, A., Young, A. K., et al. 2020, Science, 369, 1233
Larwood, J. D., Nelson, R. P., Papaloizou, J. C. B., & Terquem, C. 1996, MNRAS, 282, 597
Liska, M., Hesp, C., Tchekhovskoy, A., et al. 2021, MNRAS, 507, 983
Lodato, G., & Price, D. J. 2010, MNRAS, 405, 1212
Lodato, G., & Pringle, J. E. 2007, MNRAS, 381, 1287
Lubow, S. H., & Ogilvie, G. I. 2000, ApJ, 538, 326
Marino, S., Perez, S., & Casassus, S. 2015, ApJL, 798, L44
Martin, R. G., Zhu, Z., & Armitage, P. J. 2020, ApJL, 898, L26
Muro-Arena, G. A., Benisty, M., Ginski, C., et al. 2020, A&A, 635, A121
Nixon, C., & King, A. 2016, in Lecture Notes in Physics, Berlin Springer Verlag, ed. F. Haardt, V. Gorini, U. Moschella, A. Treves, & M. Colpi, Vol. 905, 45, doi: 10.1007/978-3-319-19416-5_2
Nixon, C., King, A., & Price, D. 2013, MNRAS, 434, 1946
Nixon, C., King, A., Price, D., & Frank, J. 2012, ApJL, 757, L24
Ogilvie, G. I. 1999, MNRAS, 304, 557
—. 2008, MNRAS, 388, 1372
—. 2018, MNRAS, 477, 1744
Ogilvie, G. I., & Latter, H. N. 2013a, MNRAS, 433, 2403
—. 2013b, MNRAS, 433, 2420
Paardekooper, S.-J., & Ogilvie, G. I. 2019, MNRAS, 483, 3738
Panić, O., van Dishoeck, E. F., Hogerheijde, M. R., et al. 2010, A&A, 519, A110
Papaloizou, J. C. B., & Lin, D. N. C. 1995, ApJ, 438, 841
Papaloizou, J. C. B., & Pringle, J. E. 1983, MNRAS, 202, 1181
Pineda, J. E., Quanz, S. P., Meru, F., et al. 2014, ApJL, 788, L34
Pringle, J. E. 1992, MNRAS, 258, 811
Rabago, I., Zhu, Z., Lubow, S., & Martin, R. G. 2024, MNRAS, 533, 360
Raj, A., Nixon, C. J., & Doğan, S. 2021, ApJ, 909, 81
Shakura, N. I., & Sunyaev, R. A. 1973, A&A, 24, 337
Sorathia, K. A., Krolik, J. H., & Hawley, J. F. 2013, ApJ, 768, 133
Stolker, T., Sitko, M., Lazareff, B., et al. 2017, ApJ, 849, 143
Stone, J. M., Tomida, K., White, C. J., & Felker, K. G. 2020, ApJS, 249, 4
Tanaka, H., Takeuchi, T., & Ward, W. R. 2002, ApJ, 565, 1257
Winter, A. J., Benisty, M., Izquierdo, A. F., et al. 2025, arXiv e-prints, arXiv:2507.11669
Zhu, Z. 2019, MNRAS, 483, 4221

DRAFT